MRI of chemical reactions and processes

Britton, Melanie M.

[Link to publication on Research at Birmingham portal](#)

Accepted Manuscript

MRI of chemical reactions and processes

Melanie M. Britton

MRI of chemical reactions and processes

Melanie M. Britton

School of Chemistry, University of Birmingham, Birmingham B15 2TT, UK.

Abstract

As magnetic resonance imaging (MRI) can spatially resolve a wealth of molecular information available from nuclear magnetic resonance (NMR), it is able to non-invasively visualise the composition, properties and reactions of a broad range of spatially-heterogeneous molecular systems. Hence, MRI is increasingly finding applications in the study of chemical reactions and processes in a diverse range of environments and technologies. This article will explain the basic principles of MRI and how it can be used to visualise chemical composition and molecular properties, providing an overview of the variety of information available. Examples are drawn from the disciplines of chemistry, chemical engineering, environmental science, physics, electrochemistry and materials science. The review introduces a range of techniques used to produce image contrast, along with the chemical and molecular insight accessible through them. Methods for mapping the distribution of chemical species, using chemical shift imaging or spatially-resolved spectroscopy, are reviewed, as well as methods for visualising physical state, temperature, current density, flow velocities and molecular diffusion. Strategies for imaging materials with low signal intensity, such as those containing gases or low sensitivity nuclei, using compressed sensing, para-hydrogen or polarisation transfer, are discussed. Systems are presented which encapsulate the diversity of chemical and physical parameters observable by MRI, including one- and two-phase flow in porous media, chemical pattern formation, phase transformations and hydrodynamic (fingering) instabilities. Lastly, the emerging area of electrochemical MRI is discussed, with studies

presented on the visualisation of electrochemical deposition and dissolution processes during corrosion and the operation of batteries, supercapacitors and fuel cells.

Contents

1. Introduction

Nuclear Magnetic Resonance (NMR) spectroscopy is fully established in chemistry and biochemistry as the preeminent analytical technique used in the determination of molecular structure and dynamics. However, as data are acquired non-invasively and the NMR signals from reactants, products and intermediates can be isolated and quantified, NMR is increasingly used to monitor chemical reactions, leading to greater understanding of reaction pathways and kinetics for a broad variety of reactions [1-4]. Reaction monitoring can be performed in a closed system, with the reaction simply contained within an NMR tube, or in an open system, where the reaction mixture is pumped inside the NMR probe, either continuously, as is done for online reaction monitoring, or introduced in batches, as is done for stopped-flow and rapid-injection reaction monitoring [3]. For all of these methods, it is expected that the reaction mixture contained within the NMR probe is well-mixed and uniform. However, there are situations where the distribution of reactants, and/or kinetics, of a reacting system may not be homogeneous, for example when the reaction couples with hydrodynamics, the reaction medium is heterogeneous or the

3

reaction is sensitive to perturbation. In such circumstances, it becomes useful to be able to spatially map, and quantify, chemical species and their physical environment. This can be achieved in NMR by applying magnetic field gradients, which spatially locate the NMR signal and are the basis of magnetic resonance imaging (MRI).

While MRI is a well-established analytical technique in biomedical research and clinical diagnosis, its ability to visualise the composition and behaviour of materials makes it well-suited to the study of spatially heterogeneous chemical reactions and processes [5-9]. MRI is able to selectively detect individual chemical components, through selection of the NMR active nucleus studied or of a specific resonance frequency (chemical shift). In addition to this chemical discrimination, it can also distinguish regions of different physical states or properties, and has been applied to the study of chemical reactors [8-11], biofilm growth [12-16], polymerisation reactions [17-19], chemical pattern formation [20, 21] and, more recently, electrochemical processes [5, 8, 9, 22].

2. Spatially Heterogeneous Chemical Reactions

Typically, it is expected that the distribution of chemical components within a reaction mixture will tend towards homogeneity, due to the driving force of entropy and the second law of thermodynamics. However, in systems far from equilibrium, it is possible for concentration gradients to develop. Open systems, such as a continuously-fed chemical reactor, are maintained far from equilibrium through the constant flow of reactants and products. In packed-bed reactors (PBRs), a concentration gradient is established axially, by the conversion of reactants into products, as the reaction mixture flows from inlet to outlet [23, 24]. Where the flow behaviour within the reactor is no longer plug-like, the conversion, and even selectivity, of the reaction can also vary across transverse sections of the reactor [23]. Identification, and control, of these concentration gradients is critical to

4

the conversion, selectivity, and hence yield, of reactions within packed-bed reactors. The optimisation of the chemical processes within a reactor requires detailed information concerning how reaction couples with flow, which in turn is influenced by the connectivity and tortuosity of channels within the reactor.

Concentration gradients can also form in closed systems, from an initially homogeneous distribution of reactants. This is observed in systems sensitive to perturbation, such as excitable reaction media, where there is a coupling between diffusion and reactions involving autocatalytic or positive feedback steps [25]. Chemical waves can form when an autocatalytic process is initiated locally, which results in a rapid, but initially, localised increase in the concentration of autocatalyst. As the autocatalyst diffuses to neighbouring regions, there is a spreading of the autocatalytic process to these regions, leading to the propagation of a chemical front. Where multiple autocatalytic steps can be sustained by the reaction media, multiple travelling chemical waves can form. The most famous example of this type of reaction is the Belousov-Zhabotinsky (BZ) reaction [26], which produces a rich variety of chemical patterns in unstirred vessels. When this reaction was first reported, it was initially dismissed, because temporal oscillations within a closed system were believed to break the second law of thermodynamics. Of course, the observed periodic changes in colour do not break the second law of thermodynamics, because they are caused by oscillations in the concentration of reaction intermediates as the reaction progresses towards equilibrium. Since its initially contentious beginnings, this reaction has become the most studied pattern-forming reaction, and provides a useful device for observing the coupling between reaction with molecular transport [21] and other environmental factors or external stimuli [27]. The chemical waves formed in the BZ reaction, and other autocatalytic reactions, are particularly useful for characterising transport and mixing behaviour within complex flow environments [28-32], because only

5

small amounts of the autocatalyst are required to enter a region, before there is a rapid amplification of the concentration of that, and associated, species.

Other examples where concentration gradients emerge within a closed system are found in electrochemical cells, where different half-cell reactions occur at the anode and cathode, and gradients in the concentration of electroactive species can arise in the vicinity of either electrode. Understanding the kinetics of electrochemical reactions, the transport of electroactive species, and the microstructure of the electrodes is of critical importance in developing electrochemical technologies within the areas of energy storage, metal finishing and the prevention of corrosion. However, these types of system pose significant challenges for MRI due to the presence of electrically-conducting materials, which can lead to problems due to radiofrequency (RF) losses and heating of the electrolyte, and of bulk metals, which can lead to undesirable variations in the RF and magnetic fields. Hence, there are currently few papers in the literature reporting MRI of electrochemical cells. However, these recent papers have demonstrated that it is possible to overcome the experimental challenges, and as MRI is able to provide unique information on local composition and transport electrochemical cells, non-invasively, in situ and in real-time, this field is set to expand substantially.

This review article will provide a brief overview of the basics of MRI and image contrast, but refers the reader to a number of excellent books [9, 33, 34] for further information on the technique. This article will focus on how MRI can be employed to visualise spatially heterogeneous chemical reactions and processes, as well as identifying and quantifying external environmental factors which influence the rate of reaction and the distribution and transport of reactants and products. A broad range of applications will be discussed, which demonstrate how MRI can be used to observe the formation, evolution and control

of chemical concentration gradients [16] within a reaction, and how this unique and quantitative information is important for understanding the underlying molecular behaviour and optimisation of chemical processes across this diverse range of systems.

3. The Basics of Magnetic Resonance Imaging

When NMR active nuclei (with non-zero nuclear spin: $I \neq 0$) are placed in a static magnetic field (B_0), they precess at a frequency (ω) dependent on the magnetogyric ratio (γ) of the nucleus and the magnitude of B_0. By applying a magnetic field gradient, G_i, (where $i = x, y, z$ and $G_i = dB_0/di$), the precessional frequency of nuclei becomes dependent on their position, r_i, along the direction of the gradient:

$$\omega(r_i) = \gamma(B_0 + G_i \bullet r_i) \tag{1}$$

While the Larmor frequency, $\omega(r_i)$, in Eq. 1 should be negative, for simplicity, this has been neglected and subsequent equations are presented so that they are consistent with this. The NMR signal, for a small volume element, dV, at position r, is proportional to the local spin density $\rho(r)$, and, as the proportionality constant has no spatial dependence, we can write:

$$dS(G, t) = \rho(r)dV \exp[i(\gamma B_0 + \gamma G \bullet r)] \tag{2}$$

The net signal, in the heterodyne detection frame, can be written as:

$$S(k) = \iiint \rho(r) \exp[i2\pi k \bullet r] \, dr \tag{3}$$

7

where k is the reciprocal space vector [35] conjugate to r and given by $(2\pi)^{-1}\gamma Gt$, with t the evolution time. $S(k)$ is measured in the time domain and inverse Fourier transformation of the signal yields $\rho(r)$, in the frequency domain, which can be considered as a three-dimensional spectrum of $S(k)$:

$$\rho(r) = \iiint S(k)\exp[-i2\pi k \bullet r]\,\mathrm{d}k \qquad (4)$$

Where k-space is traversed in time, the NMR signal is acquired in the presence of a constant magnetic field gradient and the signal sampled at successive time intervals (*frequency encoding*). Where k-space is traversed by gradient magnitude, a series of magnetic field gradient pulses are applied for a constant period prior to signal acquisition, resulting in the magnetisation of spins at different positions acquiring different phases (*phase encoding*), due to the spatially-dependent precessional frequencies imposed during the gradient pulses. One-dimensional (1D) profiles are acquired when only a single magnetic field gradient is applied, and 2- or 3-dimensional (2D or 3D) images can be acquired by applying magnetic field gradients in two or three directions, respectively. As frequency-encoding enables k-space to be sampled from a single excitation, it is typically desirable to use a combination of both frequency and phase encoding gradients when acquiring 2D and 3D images, thus minimising experiment time. In the case of 2D and 3D imaging, the experiment time is predominantly controlled by the repetition time and the number of phase-encoding steps (which generally acquire one line of the k-space raster per excitation). To speed up 2D and 3D data collection, the magnetisation can be refocused, when the T_2 relaxation time of the material permits, after each acquisition, so that multiple lines of k-space are collected per excitation. Widely-used pulse sequences of this type include Echo Planar Imaging (EPI) [36] and Rapid Imaging with Refocused Echoes (RARE) [37]. For 2D images, it is generally necessary to also apply some slice

selection to the imaging sequence, so that data are not summed along the third dimension. This is achieved by applying a gradient at the same time as a frequency-selective pulse, allowing the signal to be either selectively excited or 'crushed'. Image resolution (pixel size) and slice thickness are determined by gradient strength and generally limited by the spin density, T_2 relaxation time and mobility of spins. Typically, pixel sizes for MR micro-imaging (microscopy) systems, equipped with a vertical bore magnet, are in the range $20 - 200$ μm, with sample sizes ≤ 10 mm in a standard-bore (52 mm) magnet, ≤ 30 mm in a wide-bore (89 mm) magnet and ≤ 60 mm in a super wide-bore (154 mm) magnet.

Imaging experiments are generally based on either spin or gradient echo pulse sequences [33], which limit the reduction in signal through the dephasing caused by the gradients and, in the case of radiofrequency (RF) refocused (spin) echoes, chemical shift and magnetic field inhomogeneities. Gradient echo sequences, such as FLASH [38], benefit from using low-flip angle RF excitation pulses, allowing the repetition time to be reduced, leading to shorter experiment times. Also, as there is no need for a second refocusing RF pulse, shorter echo times are possible. A disadvantage of gradient-echo sequences is that they are sensitive to magnetic field inhomogeneities; hence, spin echo imaging sequences are more commonly used in heterogeneous environments such as packed bed reactors. In the fast spin echo sequence RARE imaging [37], multiple spin echoes are acquired following excitation, producing T_2-weighted images in times on the order of seconds.

3.1 Multinuclear MRI

While the gross selection rule, $I \neq 0$, is the primary factor determining which nuclei can be imaged by MRI, other factors also need to be taken into consideration. Indeed, even though there are many elements with NMR active isotopes, relatively few are studied by

MRI. The sensitivity of a nucleus constrains the amplitude of the NMR signal, fundamentally limiting the image resolution possible, and is proportional to its gyromagnetic ratio (signal $\propto \gamma^3$), its natural abundance, and the strength of the static magnetic field (signal $\propto B_0^2$). Hence, the ^{1}H nucleus (which has $I = \frac{1}{2}$) has the highest relative sensitivity compared to other NMR active nuclei, because it has the highest γ value, after tritium (^{3}H), and high natural abundance (~ 100%), as well as being found in water and most organic molecules. Thus, for all of these reasons, ^{1}H MRI is most commonly performed, with the vast majority of MR images being of water, particularly in biomedical MRI. Other nuclei with relatively high sensitivities include ^{19}F, ^{13}C, ^{7}Li, ^{31}P, ^{23}Na and ^{11}B. However, of these nuclei, most are either of low natural abundance or are not widely found in materials or molecules of interest. While carbon is present in all organic molecules, its NMR active nucleus, ^{13}C, is of low natural abundance (ca. 1%); hence, ^{13}C MRI is not commonly performed and samples often require isotopic enrichment, which is expensive and labour-intensive, or some type of signal enhancement [23, 39, 40]. As the ^{19}F nucleus benefits from 100% natural abundance, has a relatively high sensitivity and has $I = \frac{1}{2}$, ^{19}F MRI, as such, is not technically demanding. However, there are significantly fewer compounds containing ^{19}F, making its application more challenging and limiting its widespread use. However, the use of fluorinated compounds still offers useful opportunities for imaging with chemical selectivity. The next most sensitive nucleus is ^{31}P, which has $I = \frac{1}{2}$ and 100% natural abundance. The biological significance of molecules containing ^{31}P has led to a number of biomedical studies involving ^{31}P MRI [41]. However, despite its favourable NMR properties and sensitivity to temperature and pH [42], ^{31}P MRI has not been applied to chemical systems.

In addition to the relative sensitivity of a nucleus, the two remaining practical factors influencing the suitability of a nucleus for MRI are the intrinsic spectral line width,

determined by the T_2 relaxation time, and the minimum repetition time allowed by the T_1 relaxation time of the spin. Thus, quadupolar nuclei (where $I > 0$), which typically have short T_2 relaxation times and broad lines, can be particularly challenging to study by MRI. Of the nuclei which are quadrupolar, [7]Li has been successfully employed for MRI, as [7]Li has a relatively small quadupolar constant, and hence its lines are not prohibitively broad. It also has high natural abundance and relatively high sensitivity, and is particularly beneficial for imaging lithium-ion batteries [43, 44]. [23]Na has 100% natural abundance, but has a lower γ and, because its quadrupolar constant is larger than that of [7]Li, has significantly shorter T_2 relaxation times. As a result, it is more challenging to get high-resolution images in [23]Na MRI. However, the quadrupolar moment of [23]Na makes this nucleus particularly useful for observing molecular alignment [45, 46]. This has also been found for studies using [2]H [47, 48]. Of the remaining NMR-active nuclei, most are quadrupolar with low sensitivity and short T_2 relaxation times or long T_1 relaxation times, making them less amenable to MRI, though there are examples of MRI of ^{2}H, [27]Al, [14]N [33, 49, 50].

3.2 Image Contrast

Image signal intensity is dependent on the spin density of nuclei within each pixel (Eq. 3) and hence image contrast is fundamentally produced by variations in $\rho(\mathbf{r})$. Using this principle, it is possible to map the distribution of water in a packed bed of glass beads, where the glass beads appear invisible. It is also possible to selectively, and separately, map the distributions of a protonated liquid and a fluorinated gas in a two-phase flow reactor [51]. However, where the spin density of a sample is uniform, as is the case for a bulk liquid, it is necessary to use additional physical or chemical parameters to produce image contrast, through modulation of the intensity or phase of the NMR signal. The most common of these are T_1 and T_2 relaxation times, molecular motion (flow and diffusion) and

chemical shift. Relaxation time contrast is most commonly employed to produce image contrast in biomedical MRI, where it is most frequently used to distinguish between different tissues. However, it also offers opportunities to visualise variations in chemical composition, particularly where paramagnetic species are present. While the T_1 and T_2 relaxation of a solvent can change with composition, they typically provide an indirect measure of the composition. For more specific information on composition, chemical shift imaging tends to be more informative, though it can be more time-consuming to perform.

3.2.1 Chemical Shift Imaging

The chemical shift is the primary parameter used in NMR spectroscopy for the identification of molecular structure. In MRI, it can also be used to identify different molecules and make it possible to map their distribution within a sample. This can be done, most simply, by incorporating a frequency-selective 'soft' pulse (e.g. SECSI [52]) to selectively excite (or suppress) the signal of selected molecules with a specific chemical shift. Greater spatially-resolved information on the composition of materials is obtainable by acquiring a spectrum for each voxel in an image, which is known as spectroscopic imaging or chemical shift imaging (CSI). In these experiments, spatial information must only be acquired through phase encoding, letting the frequency dependence of the acquired data be associated purely with the chemical shifts of spins within each voxel. However, this additional spectral information increases the dimensionality of the data set, in addition to the n spatial dimensions, making these experiments more time-consuming. Also, CSI data sets tend to be significantly larger than for other types of imaging, because the number of data points collected in the spectral dimension is generally significantly greater than the spatial dimensions (e.g. 1024 – 4096 in the spectral domain compared to 64 – 256, per axis, in the spatial domain).

If the demands of the reacting system do not lend themselves to full spectral imaging, one other popular method for acquiring spatially-resolved information on chemical composition is volume selective spectroscopy (VOSY) [53, 54]. In a VOSY experiment, the NMR signal is spatially located, through selective excitation of a volume within a sample, enabling the collection of high-resolution NMR spectra from this selected region. There is a variety of ways in which the signal can be spatially located [34], which differ primarily in how the selective pulses and magnetic field gradients are applied and combined, and in whether the signal selectively excites a desired volume or suppresses undesired regions. One of the most widely adopted methods uses imaging gradients to excite three orthogonal slices, thus selecting a volume at the intersection between all three slices [54]. This method has been used to study chemical reactions inside fixed- (packed-) bed reactors [24, 55].

3.2.2 Relaxation Time Contrast

Spin-lattice (T_1) and spin-spin (T_2) relaxation are the two processes by which a perturbed spin system returns to thermal equilibrium, following excitation by RF radiation. T_1 relaxation determines the rate at which spin populations return to equilibrium and T_2 determines the rate at which the transverse magnetisation decays to zero. There are various mechanisms that contribute to magnetic resonance relaxation, which are explained in more detail elsewhere [56-58]. The principal relaxation mechanism for $I = \frac{1}{2}$ nuclei, such as ^{1}H, in liquid samples is dipole-dipole (DD) relaxation, which arises from the through-space interaction between neighbouring magnetic nuclei. Where thermal motion causes a time-dependent fluctuating magnetic field, with a component at the Larmor frequency, relaxation will occur, returning the population distribution of spin states back to thermal equilibrium following excitation by RF pulses. Chemical shift anisotropy (CSA) becomes more important at high magnetic fields and for nuclei such as ^{13}C and [19]F. For nuclei with $I > \frac{1}{2}$, quadrupolar relaxation is significantly more important than DD or CSA, which is why

quadrupolar nuclei tend to have short T_1 and T_2 relaxation times. The typically short relaxation times of most quadrupolar nuclei make them more challenging to image. Despite these difficulties, quadrupolar nuclei can also provide additional useful information about molecular orientation [45, 46] and symmetry [59].

Relaxation time contrast is introduced by optimising imaging parameters for a sequence, such as the echo time (T_E), which is the time between the excitation pulse and signal acquisition, or repetition time (T_R), which is the time between successive sequence repetitions. For a spin echo image, the intensity of signal ($a_H(\boldsymbol{r}, T_R, T_E)$) at position $\boldsymbol{r}$, is given by Eq. 5. There will be signal loss when $T_2 \lesssim T_E$ or when $T_R \lesssim T_1$. By keeping T_R long compared to T_1 and T_E short compared to T_2, a spin density image can be produced. However, by shortening T_R or lengthening T_E, it is possible to produce T_1- or T_2- weighted images, respectively. By collecting a series of images and varying either the echo time or repetition time (or applying an inversion recovery pulse and delay at the start of an imaging sequence), it is possible to produce T_2 and T_1 maps, respectively, for a system.

$$a_{\mathrm{H}}(\boldsymbol{r}, T_{\mathrm{R}}, T_{\mathrm{E}}) = M_0(\boldsymbol{r}) \left[1 - \exp\left\{ -\frac{T_{\mathrm{R}}}{T_1(\boldsymbol{r})} \right\} \right] \exp\left\{ -\frac{T_{\mathrm{E}}}{T_2(\boldsymbol{r})} \right\} \qquad (5)$$

Relaxation times are useful for identifying regions of different physical state, density or viscosity, through differences in the tumbling rate of molecules in these regions, which influence the rate of relaxation of nuclei within these molecules. T_1 and T_2 relaxation times are also useful for identifying variations in chemical composition and are affected by the presence and concentration of dissolved oxygen or ions [60, 61], particularly if the latter are paramagnetic [62-65], such as Co^{2+}, Mn^{2+}, Cu^{2+} or Fe^{3+}. DD relaxation becomes very efficient in the presence of paramagnetic species, due to the significantly larger magnetic

14

moment of unpaired electron spins, which is ~10^3 times larger than nuclear magnetic moments. The extent to which they affect the relaxation time of surrounding molecules is determined by the relaxivity, r_1 or r_2, of the paramagnetic species [66], which in turn is dependent on the number of unpaired electrons of the paramagnetic ion, the number of co-ordinated water molecules (q), the distance between the water protons and the unpaired electron spin (r), the rotational correlation time of the ion/complex (τ_R), the electron spin relaxation time (T_{1e}), the residence lifetime of co-ordinated water molecules (τ_M) and the resonance frequency of the nucleus (ω). As relaxation rates ($1/T_i$, where $i =$ 1,2)) are additive, the influence of the paramagnetic species on the relaxation rate of the solution, is also dependent on the intrinsic (diamagnetic) relaxation rate of the solvent $(1/T_i)_{solvent}$.

$$(1/T_i)_{solution} = (1/T_i)_{solvent} + r_i[M] \tag{6}$$

The relaxivity of the paramagnetic species can be determined from a plot of $(1/T_i)_{solution}$ as a function of its concentration [M] (Eq. (6)). While the development of contrast agents of increasing relaxivity is a major focus in medical imaging [67], the use of paramagnetic contrast agents is also of relevence in the imaging of chemical reactions. By knowing the relaxivity of a paramagnetic species and the relaxation rate of the solvent, it is possible to accurately determine the concentration of the paramagnetic species, which can also then be mapped [62, 63, 66]. Where reactions involve paramagnetic species, it becomes possible to directly monitor the progress of that reaction [63, 68]. The relaxation of water molecules co-ordinated with a paramagnetic ion has also been found to be sensitive to changes in the structure of the complex [69].

While paramagnetic ions have a significant effect on the relaxation time of surrounding molecules, diamagnetic ions also influence solvent relaxation times, though typically requiring molar concentrations, rather than millimolar [61], before their presence becomes noticeable. The influence can be through changes in the viscosity of the solution, or through complexation with solvent molecules. In aqueous solutions, diamagnetic ions are known to either increase or decrease the relaxation times of water molecules, with increasing ion concentration, via changes in mobility of surrounding water molecules [70]. Whether a dissolved ion increases or decreases the mobility of solvent molecules, and hence its influence on solvent relaxation times, depends on whether the ion is 'structure-breaking' or 'structure-making' [61]. Structure-making (*kosmotropic*) ions, such as Li^+ and Na^+, co-ordinate with water and hence decrease the mobility of surrounding water molecules, leading to a decrease in relaxation time, as the concentration of ions increases. Structure-breaking (*chaotropic*) ions, which increase the mobility of water molecules and hence increase the relaxation time of water, are less common than structure-making ions and generally restricted to large monovalent ions, such as Rb^+, Cs^+, NO_3^-.

Another important chemical influence on relaxation times is chemical exchange, particularly through proton exchange between water and hydroxyl or amide groups. The measured values for both T_1 and T_2 are affected by the exchange rate ($1/\tau$) of spins between different chemical environments [71, 72]. T_2 is also affected by the difference in chemical shift ($\Delta\omega$) between the two environments. Where the exchange rate is fast ($1/\tau \gg \Delta\omega$), a single resonance is observed for the exchanging spins and their relaxation times are averaged. At intermediate exchange rates ($1/\tau \approx \Delta\omega$), broader spectral lines occur, which correspond to rapid signal decay. As the rate of exchange is affected by pH and concentration, it therefore becomes possible to monitor these quantities through measurements of the T_2 relaxation time of a reacting solution. This has been successfully

16

applied to the determination of hydrogen peroxide concentration [73], and to the measurement of pH in the aqueous environment of a reverse microemulsion [74]. Molecules containing protons that readily exchange with the protons in the water pool have been used as T_2-contrast agents in MRI [75-77]. The T_2 contrast can be made even more pronounced by applying RF radiation at the frequency of the exchangeable protons of the contrast agent, and is the basis for Chemical Exchange Saturation Transfer (CEST) imaging [77, 78]. The T_2 contrast can be still further increased when protons exchange with a contrast agent that is hyperpolarized (HYPERCEST) [79], or is paramagnetic (PARACEST) [80], which typically increases $\Delta\omega$ between the exchanging resonances.

3.2.3 Flow and Diffusion

A major influence on the distribution of chemical species, and the rate of reaction, is translational motion, such as flow (coherent motion) and/or diffusion (incoherent motion), which can be measured using the pulsed gradient spin echo (PGSE) sequence. More detailed texts on the PGSE experiment, and measurement of flow and diffusion in general, can be found elsewhere [81, 82]. In brief, the PGSE pulse sequence contains two narrow magnetic field gradient pulses, of equal duration, δ, and amplitude, $\boldsymbol{G}_{\Delta}$, on either side of a 180˚ refocusing RF pulse. Translational motion of spins during the observation time, Δ, between the two gradient pulses, results in a phase shift, ϕ, of their NMR signal. The distribution of mean-squared displacements for self-diffusing molecules results in a distribution of phase shifts which is dependent on $\boldsymbol{G}_{\Delta}$, δ, Δ, and the self-diffusion coefficient, D. It is this distribution of phase shifts that leads to an attenuation of the overall NMR signal, which is typically measured over a range of $\boldsymbol{G}_{\Delta}$ values, keeping δ and Δ constant. The diffusion coefficient is then determined by fitting the signal decay to the Stejskal-Tanner equation (Eq. (7)) [83]:

17

$$\frac{S(\boldsymbol{G}_\Delta)}{S(0)} = \exp[-\gamma^2\delta^2 G_\Delta^2 D(\Delta - \frac{\delta}{3})] \tag{7}$$

where $S(\boldsymbol{G}_\Delta)$ is the measured signal intensity and $S(0)$ is the signal intensity when $\boldsymbol{G}_\Delta = 0$.

An alternative analysis of this data is to Fourier transform the signal, $S(\boldsymbol{G}_\Delta)$, with respect to

q (where $q = \gamma\boldsymbol{G}_\Delta\delta/2\pi$), resulting in an averaged propagator, $P(\boldsymbol{R}, \Delta)$, which describes the

probability that spins will displace a distance $\boldsymbol{R}$ over the observation time, Δ, [81]:

$$S(\Delta, q) = S(0)\int_{-\infty}^{+\infty} P(\boldsymbol{R}, \Delta)\exp(-iq\boldsymbol{R})d\boldsymbol{R} \tag{8}$$

where the propagator for free diffusion is a Gaussian function:

$$P(\boldsymbol{R}, \Delta) = (4\pi D\Delta)^{-3/2}\exp(-\boldsymbol{R}^2/4D\Delta) \tag{9}$$

In the case of flow, where molecular motion is coherent, the NMR signal will gain a net

phase shift, φ, which is dependent [33] on $\boldsymbol{G}_v$, δ, Δ, and the flow velocity $\boldsymbol{v}$:

$$\varphi = \gamma\boldsymbol{v}G_\Delta\delta\Delta \tag{10}$$

In order to image translational motion, it is necessary to incorporate two motion-encoding

(PGSE) gradients into the imaging sequence. Velocity and diffusion coefficients are

measured in the direction of the applied PGSE magnetic field gradient, and in the case of

complex flow it may be necessary to acquire images with flow encoding in multiple

18

directions [84, 85]. Diffusion maps are typically acquired over a range of motion-encoding gradients (typically ≥ 8). In the case of flow, it is possible to determine the velocity within each voxel by the measuring the phase shift between two images measured with different PGSE gradient amplitudes (G_Δ). An alternative method is to acquire velocity images from a greater number of PGSE gradient values, or q-slices, (typically 8 or 16) and Fourier transforming, with respect to q, resulting in a propagator for each voxel in the image. This method is able to determine both the velocity, from the displacement of the peak maximum, and the root mean squared displacement due to diffusion and dispersion, from the width of the propagator. While this second method results in longer experiment times, from the increased number of q-slices, it is useful for observing fluctuations in velocity [86]. Both flow and diffusion can be measured in the same experiment; however, the PGSE parameters are optimised slightly differently for the two properties. In the case of diffusion measurements, the signal is often attenuated to a value approximately $S(G_\Delta)/S(0) \lesssim 0.01$, and the PGSE parameters are chosen to achieve this, within any sample-specific constraints. The precision of flow measurements can be optimised by maximising the phase shift, subject to a maximum value of 2π to avoid aliasing in the velocity measurement.

4. Visualising Chemical Waves and Fronts

Chemical fronts and patterns, produced by autocatalytic, clock or oscillatory chemical reactions, can be readily visualised by MRI when the reaction involves a change in the oxidative state of a paramagnetic species, typically a transition metal, which is accompanied by a change in the number of unpaired electrons and, hence, relaxivity of the species. By varying T_E and T_R, to optimise T_1 or T_2 contrast, it is possible to visualise the chemical waves or fronts through the differences in relaxation time of the solvent at the wave/front, compared to the surrounding medium [87]. Using this method, a variety of

19

autocatalytic reactions have been investigated, including the chemical waves formed in the BZ reaction [87, 88], and its analogues [68], and the chemical fronts formed in the reactions between Co(II)EDTA^{2-} with hydrogen peroxide [64] and Fe(II) with nitric acid [65]. While these reactions may also produce chemical waves which are visible optically, MRI has the advantage of being able to observe them in opaque environments, such as a packed bed (Fig. 1).

<Figure 1 near here>

Also, as there is a direct relationship between solvent relaxation time and signal intensity, knowing the relaxivity of a paramagnetic species and its concentration, it is possible to quantitatively map the concentration of the species [89]. This can be through the acquisition of relaxation time maps [15, 62] or, where a system evolves rapidly and requires fast data acquisition, directly from a relaxation-weighted image [63]. This method has been used to map the concentrations of Mn^{2+} and Mn^{3+} ions in chemical waves (Fig. 2) formed in an analogue of the BZ reaction [63], of Co^{2+} in a biofilm-mediated ion exchanger [90] and of Cu^{2+} near a corroding copper strip [62] or immobilised within a biofilm [15].

<Figure 2 near here>

While the patterns formed in the BZ reaction have been those most studied by MRI, in a variety of environments (see sections 5.1 and 5.2), there are a number of other chemical wave systems that have suitable characteristics for study by MRI. Of these, the chemical front produced by the reaction between Co(II)EDTA^{2-} and H$_2$O$_2$ is particularly well-suited to MRI, because the unreacted solution contains paramagnetic Co^{2+} ions and the reacted

solution contains diamagnetic Co^{3+} ions, resulting in a large T_2 relaxation difference

between the two solutions (T_2 = 398 ms (0.02 M Co(III)EDTA⁻ solution); T_2 = 33 ms (0.02

M Co(II)EDTA²⁻ solution)). When this reaction is studied in vertical tubes, the shape of the

front produced when the reaction is locally initiated, by the addition of a small amount of

hydroxide solution, is dependent on the direction of propagation with respect to gravity.

When the front is initiated at the bottom of a tube, the front propagates upwards with a flat

interface. However, if the front is initiated at the top, the initially flat interface soon

develops into a chemical finger, due to density differences between the reacted (more

dense) and unreacted (less dense) solutions. It has been found that this reaction can also

be controlled by the application of magnetic field gradients [91], and that the magnetic field

gradients of the MRI instrument can be used not only to image the chemical fronts, but

also to control the velocity [64] and direction [92] of the front by applying a series of

gradients, applied over a period of time, in a specific direction. Where a magnetic field

gradient is applied parallel to the direction of the propagating front [64], the front is

accelerated as it travels down the field gradient, but slows when it travels up. It is also

found that, when magnetic field gradients are applied normal to the direction of front

propagation, the leading edge of the front can be directed [92] (Fig. 3), so that the position

where the chemical finger forms can be precisely controlled, and the finger can be made to

switch from one side of the tube to the other.

<Figure 3 near here>

The change in magnetic properties between reacted and unreacted states also makes this

reaction a suitable candidate for investigation by superconducting quantum interference

devices (SQUIDs) [69], which enable the transition from a paramagnetic solution,

containing Co(II)EDTA²⁻ ions, to a diamagnetic solution, containing Co(III)EDTA⁻ ions, to

21

be monitored as the reaction 'clocks' (Fig. 4(a)). This monotonic transition is also detected in measurements of pH (Fig. 4(b)). However, it is the T_2 relaxation time of the solution that offers unique insight into this reaction. In contrast to other measurements made on this reaction, the T_2 relaxation time of water shows a more complex transition, with an initial slight, but temporary, increase in T_2 before the reaction clocks, marked by the rapid increase in T_2 relaxation time (Fig. 4(c)). While the origin of this behaviour is not fully understood, it has been speculated that it is due to the formation of an intermediate state which has either fewer co-ordinated water molecules (lower q) or a change in residence lifetime (τ_m) for any co-ordinated water molecules [69].

< Figure 4 near here >

5. Chemistry in Flow

While the chemical patterns of the BZ reaction are visually attractive, they also offer a visual method for probing the coupling of reaction with flow and dispersion in a variety of flow environments. Autocatalytic reactions are found to be particularly sensitive to the effects of flow and mixing, being, either amplified or extinguished by them. However, understanding the relationship between flow and reaction goes far beyond pattern-forming reactions and is central to the efficiency and selectivity of many chemical reactors.

5.1 Vortical Flow

The interplay between chemistry and flow has also been investigated in a series of counter-rotating (Taylor) vortices [29, 30, 85], formed in a Couette cell above a critical rotation rate. MRI has proved particularly useful for characterising the flow and intra-/inter-vortex mixing [93, 94] characteristics for Taylor vortices, through MRI velocity and diffusion imaging (Fig. 5(a) and (b)) and propagator measurements. When the fluid within a series

of Taylor vortices is the BZ reaction, and the autocatalysis is triggered locally, a travelling chemical wave is observed, which propagates through the vortices, initially along the outer regions of each vortex, where mixing is greatest [30], before propagating inwards, into the centre of each vortex (Fig. 5(c)). By comparing MRI measurements of molecular transport with visualisation of the chemical waves, it was shown that the rate at which a wave travels along the vortices depends on the amount of inter-vortex mixing, which is controlled by the rotation rate of the inner cylinder (Fig. 5(d)). Furthermore, it has been found that even more complex chemical patterns can be generated by controlling either the rate of reaction, or the flow velocities in the system (Fig. 5(d)) [95].

<Figure 5 near here>

MRI has recently also been used to characterise the flow and mixing behaviour of translating Taylor vortices, formed in a vortex flow reactor (VFR) when axial flow is superimposed on Taylor vortices in a Couette cell [94]. It had been assumed that under laminar flow conditions, the VFR would exhibit plug-like flow with negligible inter-vortex mixing. This would allow residence times inside the reactor to be controlled, thus making the VFR an ideal candidate for a variety of chemical and biochemical reactions [96-100]. However, there has been significant debate in the literature about the flow and mixing behavior of VFRs, and how they influence chemical reactions within a VFR. While MRI has been shown to provide detailed information about non-translating Taylor vortices, the translational motion of vortices in a VFR makes this type of flow more challenging to visualise using MRI. This is because the periodic motion of the travelling vortices causes motion artefacts in the image, requiring data acquisition to be synchronised with the motion of the vortices. In a study by Vallatos et al. [94], these motion artefacts were avoided by timing data acquisition to match the translational period of the vortices. By

23

using a combination of velocity and diffusion imaging, with bulk propagator measurements, the molecular displacement and mixing behaviour of this complex laminar flow was characterised for the first time [94]. This study showed that while the VFR has some plug-like flow properties, there is also significant mixing between neighbouring vortices, as the vortices travel along the length of the reactor, controlled by the inner cylinder rotation rate. Visualisation of the complex interplay between molecular transport and reaction is nicely demonstrated by the BZ reaction, which can be used to identify the regimes where plug-like flow is greatest or least [29].

5.2 Packed Beds

The most common reactor exhibiting plug-like flow properties is the packed-bed reactor (PBR) - a tubular reactor filled with solid catalyst particles - which is favoured for its typically high conversion rate per weight of catalyst, and widely employed in the chemical industry. However, it is known that ideal plug flow may not be the case in this type of reactor, due to higher velocity channels at the wall of the reactor, caused by the more ordered packing of catalyst particles by the reactor walls, which promotes the formation of these channels [101]. The BZ reaction has been used to directly visualise this flow heterogeneity in a PBR, requiring the use of MRI to visualise the waves in this optically opaque system. By comparing MRI velocity images of flow in the PBR with the chemical waves formed by the BZ reaction, the relationship between chemistry and local hydrodynamics within the PBR can be clearly observed [28], the conical shape of the chemical waves being caused by the lower average residence times experienced by the reacting solution close to the wall of the reactor (Fig. 6).

<Figure 6 near here>

24

Understanding the coupling between flow and chemistry in PBRs is of significant importance in the chemical industry, where improved understanding of the relationships between chemical conversion and selectivity, and of the hydrodynamics, is essential for the optimisation of catalytic processes and reactor operation. Several studies by the Gladden group [23, 24, 101] have demonstrated how MRI is able to provide *in situ* quantitative, spatially-resolved information on the relationship between local hydrodynamics and chemical conversion and selectivity for a number of reactions in packed-bed reactors. In a study of the esterification of methanol and acetic acid, in the presence of a proton-exchange catalyst, the ^{1}H chemical shift of the hydroxide group was used to monitor chemical conversion [24]. Using a combination of 1D CSI and volume selective spectroscopy, they observed an increase in conversion axially, as the reacting solution flowed towards the outlet in the PBR, as expected. However, it was also observed that there was a variation in conversion across a transverse section of the reactor, [101] (Fig. 7), with increased conversion in the centre of the PBR. This variation in conversion is caused by the increased concentration of pores with fluid flowing at higher velocities, and correspondingly lower average residence times, near the walls of the PBR, compared to the centre of the PBR where the pore space is more tortuous.

<Figure 7 near here>

The spatial dependence of chemical conversion and selectivity has also been seen in the competitive hydration and etherification reactions of 2-methyl-2-butene, across a transverse slice of a fixed-bed reactor. In this reaction, the identification of reactants and products utilised the ^{13}C NMR signal, due to the larger chemical shift range it offers. The researchers avoided having to isotopically enrich the reactants, commonly necessary because of the lower natural abundance and sensitivity of the ^{13}C nucleus, by

25

incorporating a distortionless enhancement by polarisation transfer (DEPT) sequence into the imaging sequence [23]. This methodology was later extended to look at the esterification of acetic acid with ethanol over an ion-exchange resin [102]. By using the DEPT-enhanced ^{13}C NMR signal for each carbon-containing species, they were able to selectively measure the apparent inter- and intra-particle diffusion coefficients for these species at different axial positions within the PBR. The concentration of the molecules in the inter-particle space was determined directly using spatially-resolved spectroscopy, but was estimated in the intra-particle spaces from the diffusion data. From these measurements, they were able to show that the concentration of ethyl acetate product was higher within the intra-particle pores than for the inter-particle regions, indicating that the reaction was mass-transfer limited.

5.3 Imaging gases

As many reactions in packed-bed reactors involve gases, it is useful to be able to image these, enabling a more complete overview of processes within a reactor. However, imaging gases is made more complicated by their significantly lower spin densities and, typically, shorter relaxation times [103]. Thus, MRI of gases generally requires some means of signal enhancement, such as through the use of hyperpolarised noble gases [104], para-hydrogen induced polarisation [105], or, where thermal polarisation is employed, by using gases which contain multiple spins per molecule, such as gaseous alkanes [106] or the fluorinated gases SF_6, CF_4 or C_2F_6 [107]. The rapid relaxation observed for many gases can be favourable for boosting the signal through rapid, and extensive, signal averaging. However, the short-lived signals may also require the use of pure phase-encoding imaging methods [108, 109]. Signal enhancement may also be necessary, as was employed in an investigation of the hydrogenation of propylene, where para-state enriched hydrogen gas was used to visualise the velocity and distribution of

gases [110] or temperature [105] in a PBR. Where a process involves two-phase flow, it is useful to simultaneously map both liquid and gas [51, 111]. While regions of liquid and gas can be identified using differences in spin density [84], it is more challenging to simultaneously measure the velocities of these two phases. Recently, it has been demonstrated that it is possible to simultaneously measure the velocity of both liquid and gas phases [51]. Images were collected of two-phase flow in a trickle bed reactor by employing the ^{1}H MR signal of the liquid (water) and the ^{19}F MR signal from the fluorinated gas SF_6 (Fig. 8). The lower spin density of the SF_6 limited the spatial resolution of the gas phase images, which had a pixel size of 708 μm $\times$ 708 μm (with a slice thickness of 2 mm), compared to the pixel size of 177 μm $\times$ 177 μm for the liquid images (at a slice thickness of 1 mm). However, recent advances in compressed sensing (CS) MRI [112], have made it possible to visualise two-phase flow with the same voxel dimensions for both phases [113].

<Figure 8 near here>

5.4 Compressed Sensing

In addition to its applications in studying two-phase flow (section 5.3), compressed sensing is also proving invaluable when mapping chemical composition [114] by CSI, where the additional spectral information can come at the expense of spatial or temporal resolution. By using compressed sensing, it is possible to significantly reduce experiment times and/or improve spatial (or spectral) resolution [114], even for molecules in low concentrations or for nuclei with low natural abundance and/or sensitivity (e.g. [19]F [115],[13]C [116, 117]). Using compressed sensing, Holland and co-workers were able to collect quantitative 2D concentration maps for binary mixtures of 1,4-dioxane and

27

cyclooctane [114] with an experiment time of 8 min, compared to the 17 h experiment required for a 2D chemical shift image.

5.5 Fingering instabilities in porous media

The coupling between reaction and flow can lead to hydrodynamic instabilities, such as viscous- or density-fingering [118, 119], where the reaction results in a change in viscosity or density. These instabilities, also known as Saffman-Taylor (viscous-fingering) and Rayleigh-Taylor (density-fingering) instabilities, have been observed across a variety of porous media, and occur when one fluid displaces another of different viscosity or density. The nature of the instability will depend on the orientation of the fluids with respect to each other and to gravity, and on the direction of flow. Density-fingering occurs when a more dense fluid is located above a less dense fluid and the interface between the two fluids becomes destabilised, resulting in structures known as 'fingers'. Viscous fingering occurs in a porous medium when a less viscous fluid displaces a more viscous fluid, again resulting in the formation of fingers at the interface between the two fluids. Most studies on density- and viscous-fingering instabilities have used Hele-Shaw cells, which are composed of parallel transparent glass plates separated by a narrow gap. However, while Hele-Shaw cells enable direct observation of fluids, they are unable to reproduce the connectivity and tortuosity of a real 3D porous network. As an alternative, MRI is particularly well suited to visualise the formation of fingering instabilities in porous media [6], and has been applied to a number of studies on viscous fingering [120, 121]. In these studies, the different fluids were distinguished by introducing a paramagnetic salt into one of the fluids and using relaxation time contrast to selectively suppress the signal of that fluid.

A change in density or viscosity, as a result of chemical reaction, can lead to more complex fingering behaviour, and can even induce fingering instabilities in otherwise stable configurations [122]. MRI has been used to investigate the chemical fingers formed in a packed bed as a result of the formation of a highly viscous fluid at the interface between two miscible fluids of low, but similar, viscosity. The low viscosity solutions contained either the cationic surfactant cetyltrimethylammonium bromide (CTAB) or the co-surfactant sodium salicylate (NaSal). When these two solutions mix, the surfactant and co-surfactant molecules aggregate to form wormlike micelles, resulting in a highly viscoelastic solution [71]. When either fluid is pumped, displacing the other, chemical fingers form at the interface. In this system, the three solutions, containing CTAB, NaSal or wormlike micelles, could be discerned from differences in the T_2 relaxation times of the water in the different solutions (1660 ms (CTAB), 664 ms, (wormlike micelles) and 240 ms (NaSal)), rather than relying on the introduction of a paramagnetic salt. Using these differences in T_2 relaxation times, finger formation and development was observed, as the fluids were pumped through the packed bed, as a function of flow rate.

6. Imaging Temperature Changes Caused by Reaction

A number of studies have used MRI to map temperature changes associated with chemical reactions [50, 105]. In their study of the hydrogenation of propylene [105], Bouchard et al. used para-enriched hydrogen gas to map the temperature in the pores of a PBR containing metal nanoparticles and metal–organic framework catalysts, by measuring the linewidth of the ^{1}H NMR signal, which was dependent on the temperature of the H_2 gas. An alternative method was used by Koptyug et al. [50] in their investigation of the catalytic hydrogenation of propylene, which relied on the NMR signal of the solid-phase catalyst support as a temperature probe. Using [27]Al MRI, they were able to image, in 2D, γ-Al_2O_3 catalyst beads [123], and to measure temperature profiles through a fixed bed

containing 1 mm Pd loaded γ-Al$_2$O$_3$ catalysts beads, supplied with propylene and H$_2$ gases [50]. This group has also used MRI to probe temperature changes resulting from the formation of a chemical front in the autocatalytic oxidation of thiosulfate by chlorite ions [124]. In this study, they used an echo-shifted TurboFLASH imaging sequence, which produced temperature-related phase shifts in the ^{1}H NMR signal of the water. They were able to measure temperature changes over 1 ˚C, allowing this chemical front, which cannot be imaged using NMR relaxation contrast methods, to be visualised by MRI (figure 9).

<Figure 9 near here>

7. Phase Transitions

The changes in molecular mobility caused by a phase transition can be most easily detected in MRI by changes in the relaxation time and signal intensity of the affected molecules. This is most apparent for bulk transitions between liquid and solid, such as during freezing and melting processes. MRI has been used to visualise freezing in sucrose solutions [125, 126], relying on changes in the ^{1}H MRI signal intensity to map this process.

7.1 Polymerisation reactions

Polymerisation reactions, which can result in dramatic changes in viscosity, have also been investigated by MRI [17-19]. MRI has been used to visualise acrylate polymerization [18], where there was a conversion from monomer to polymer via a localized exothermic reaction zone which then propagated through a solution of the monomer. The polymerization reaction was observed using T_2-weighted imaging, with regions of low monomer conversion appearing bright (longer T_2) and regions of high monomer conversion appearing dark (shorter T_2), due to the differing molecular mobilities in those

30

regions. 3D MRI of this system enabled the visualization of the 3D spiral structure of the single-head spin mode[18].

8 Current density and conductivity imaging

Current density and conductivity mapping by MRI enables spatial and temporal changes in the concentrations of ionic species to be monitored during chemical reactions [127] and tablet dissolution [128]. Current density imaging (CDI) experiments are based on a spin echo imaging pulse sequence, where external electrodes provide additional bipolar electric current pulses, which are applied synchronously with the imaging sequence. The intensity of the CDI is proportional to the electric current density within the sample. The sensitivity of the CDI is dependent on, in addition to the signal-to-noise of the conventional MR image, the impedance of the sample, the applied voltage, and the total duration of the electric current pulses (T_c). Electric currents produced in the sample induce an additional magnetic field component ($\boldsymbol{B}_c$), on top of the static magnetic field ($\boldsymbol{B}_0$), and cause a shift (ω_c) in the Larmor frequency, which is determined by measuring a phase shift φ_c (where $\varphi_c = \omega_c T_c$). From ω_c, the magnetic field component $\boldsymbol{B}_c$ is determined and the current density calculated using Ampere's law [128].

CDI has been used to visualise the changes in ionic concentration within an ion-releasing tablet as it dissolves, by observing conductivity changes in the gel medium surrounding the tablet. Using these measurements, diffusion constants were determined for the different acids contained in the tablet [128]. Spatially heterogeneous chemical reactions have also been mapped by CDI. The formation of calcium carbonate, by the perfusion of gaseous CO_2 in saturated calcium hydroxide solution [127], was visualized through observation of the current density, which was high in the calcium hydroxide solution, due to the presence of Ca^{2+} and OH^- ions, but, was low where $CaCO_3$ formed. Over time, the region containing

$CaCO_3$ was observed to increase, until all the calcium hydroxide was transformed into calcium carbonate. This process was then reversed by adding HCl, which caused the charge density to increase as Ca^{2+} and Cl^- ions were generated. These experiments nicely demonstrate the advantage of CDI over conventional MRI, which is typically only able to image the change in size of a dissolving tablet or the formation of a solid, rather than directly map the distribution, mobility and concentration of ions in solution.

9. Electrochemistry

A recent exciting development in MRI has been the visualisation of electrochemical dissolution and deposition processes during corrosion and battery operation [22]. Traditionally, electrochemical systems have not been widely studied by MRI due to the practical challenges of imaging systems containing bulk metals and/ or highly conducting electrolyte solutions, which can lead to undesirable variations in the RF (B_1) and B_0 fields across the sample, as well as to heating. Some of these challenges have been addressed for in situ NMR spectroscopy studies of batteries, fuel cells and supercapacitors [129-132]. Spatially-resolved spectra, and 1D concentration profiles, have been collected in fuel cells [133, 134] and lithium batteries [135-137] by rotating frame imaging using toroid cavity detectors [137, 138]. More recently, MRI studies of electrochemical cells have employed magnetic field gradient imaging methods to collect 1D concentration profiles and 2D/3D images using frequency-echo [22, 43, 44, 62, 139-142] and pure phase-encoding [143-145] imaging methods. Of these studies, a number have investigated lithium batteries, using [7]Li MRI, which benefits from the high natural abundance, relatively high sensitivity and sufficiently long NMR relaxation times of the [7]Li nucleus. [1]H MRI has been applied to investigate the dissolution and transport of copper and zinc ions [62, 139, 140], which, due to the inherently broad lines and lower sensitivity of [63]Cu/[65]Cu and [67]Zn, cannot be directly imaged by MRI. Regardless of whether the electroactive species can be imaged directly or

not, it is increasingly found that MRI is able to provide unique information, in situ and in real time, about the speciation, distribution and transport of these species, which are critical to understanding a variety of electrochemical processes and are important in the design and development of improved electrochemical technologies.

9.1 Corrosion

9.1.1 Zinc corrosion

The first reported application of magnetic field gradient MRI to study an electrochemical cell containing bulk metal was a study of the galvanic corrosion of zinc in a saturated LiCl solution [139]. Using ^{1}H MRI, a series of T_1 and T_2 maps of water in the electrolyte were collected, over a period of two days, as the zinc corroded (Fig 10), which enabled the dissolution, transport and speciation of zinc ions to be monitored. Slight image distortions due to magnetic susceptibility were observed near the metallic zinc electrode, but were minimised by embedding the metal in a plastic plug, with only the end surface of the metal wire exposed to the electrolyte, and by positioning it at the bottom of the cell. The distortions at the metal/electrolyte interface were greatest in the T_2 maps, which are especially sensitive to magnetic susceptibility artefacts. The distortions were less pronounced in the T_1 maps, which, in the early images, showed regions of significantly lower T_1 relaxation times by the edge of the zinc wire, which can be explained by the presence of dissolved Zn^{2+} ions (Fig. 10(a) and (b)). This observed decrease in T_1 time of the electrolyte occurs because Zn^{2+} is a structure-making ion [61], which reduces the mobility of any co-ordinated water molecules. The reduction in mobility of the water molecules increases their rotational correlation time, which, in turn, increases their relaxation rate ($1/T_1$) and hence decreases the T_1 in that region. As more Zn^{2+} goes into solution, however, there is not a continuing decrease in T_1 relaxation of the electrolyte in that region. Instead, an increase in T_1 was observed, that was believed to be caused by a

33

change in the speciation of the zinc ions [139], from Zn^{2+} to $ZnCl_y^{x+}$, which, as structure-breaking ions, increase the mobility of surrounding solvent molecules, leading to an increase in their T_1 relaxation time. This region of increased T_1 was found to grow and propagate towards the Pt electrode. While the T_1 relaxation time of the solvent showed the greatest contrast due to the distribution and speciation of ions, a region of reduced T_2 could also be observed ahead of the propagating front of zinc ions. The underlying molecular origins of this reduction in T_2 remain uncertain, though it has been suggested [139] that a change in water structure, which is expected in this region [146], could be responsible.

<Figure 10 near here>

9.1.2 Copper corrosion

Building on this earlier work, Britton and co-workers extended the methodology to produce quantitative 2D and 3D concentration maps, in situ and in real-time, of Cu^{2+} during the corrosion of copper [62]. In this study, metallic copper was electrochemically, and controllably, dissolved. Again, ^{1}H MRI of water in the electrolyte was used to visualise the dissolution, speciation and transport of copper ions in the cell. However, by selecting metallic strips, rather than cylindrical wires, and by orientating them so that they were parallel with both the B_0 and B_1 fields (Fig. 11 (a)), it was possible to eliminate image distortions near the metal/electrolyte interface and collect viable data immediately adjacent to the metal electrode [62, 140].

<Figure 11 near here>

A series of 2D T_1 maps was collected during the electrodissolution of copper, with the application of increasing current [62]. As Cu^{2+} is paramagnetic, MRI is particularly sensitive to its presence, with the limit of detection, in these experiments, found to be *ca.* 20 μM. The linear relationship between the concentration of Cu^{2+} and the relaxation rate, R_1, of the water (Eq. (6)), made it possible to convert the T_1 maps into Cu^{2+} concentration maps (Fig 11 (b)). By comparing the number of moles of Cu^{2+} in solution with the number expected, based on the applied current, it was found that there was excellent agreement between the two, indicating that the measurements were quantitative. However, it was noticed that after some time, the total concentration of Cu^{2+} detected in solution began to deviate from that expected, which was explained by a change in speciation of the copper from aqueous Cu^{2+} to solid CuO or CuOH, which have significantly less effect on the relaxivity of the solvent. This change in speciation is caused by the reaction between Cu^{2+} and hydroxide ions, which form at the cathode and propagate towards the anode. In the region nearest the cathode, it was also possible to detect the depletion of dissolved O_2, which is paramagnetic. The ability to map Cu^{2+} in 3D and in real time (Fig. 12) was also demonstrated by collecting 3D images with an inversion recovery delay, which could be converted into 3D T_1 maps, and subsequently 3D concentration maps [62].

<Figure 12 near here>

9.2 Batteries

9.2.1 Zinc-air batteries

The same methodological approach used to study copper corrosion (section 9.1.2) has also been applied to the investigation of zinc-oxygen electrochemistry inside a model zinc-air battery [139]. However, the electrochemistry in this system was found to be significantly more complex, and image contrast did not come directly from the distribution

and speciation of the zinc species, as in the earlier study on zinc corrosion (section 9.1.1) [139]. In these experiments, the cell comprised a 1 M NaOH electrolyte with a zinc anode and a rare-earth coated titanium cathode, which was under constant load over a period of two days. The composition of the electrolyte was monitored using ^{1}H T_1 maps of the water in the electrolyte, which were dominated by the evolving concentration of hydroxide ions. As shown in the image of a series of tubes containing a range of concentrations of sodium hydroxide ([NaOH] = 0 – 10 M) (Fig. 13(a)), T_1 decreases with increasing [OH$^-$]. During discharge of the Zn-air cell, the cathodic reaction produces hydroxide ions, decreasing the T_1 of the solvent, and the anodic reaction produces zincate ions, which decreases [OH$^-$] and hence increases the T_1 of the solvent. Images of the cell under constant load show that at the early stages of discharge (Fig. 13 (b)-(f)), the cell is behaving as expected, with transport of zincate ions away from the zinc anode and hydroxide formation at the Ti cathode. However, after several hours, regions of high and low [OH$^-$] are observed on either side of the Zn anode, indicating that the cell is failing, with both the anodic and cathodic reactions occuring on the Zn metal.

<Figure 13 near here>

9.2.2 Lithium batteries

Direct, in situ, observation of the distributions of electroactive species has been performed in lithium-ion batteries containing LiPF$_6$ electrolyte, using ^{7}Li and ^{19}F MRI [44, 144]. 1D concentration profiles of Li species from a lithium electrode in axisymmetric lithium cells have been collected using spin echo frequency-encoding [44] and phase-encoding [144] imaging methods. In the study by Klett et al. [44], ^{7}Li spin-density profiles were collected, within a symmetrical cell containing two lithium electrodes under constant current, which enabled the mapping of lithium ion concentration over time (Fig. 14), leading to the

determination of Li$^+$ transport number and diffusion coefficient. Due to the lower sensitivity of ^{7}Li, the acquisition time was 17 min for each 1D profile. In their study of a graphite−lithium metal cell, Goward and co-workers [144] used a combination of ^{7}Li and ^{19}F MRI to visualise the distributions of the Li$^+$ cations and PF$_6^-$ anions. Two advantages of using ^{19}F MRI are the increased sensitivity and the longer T_2 relaxation times of this nucleus, which lead to higher signal-to-noise and, hence, reduced acquisition times. In both of these studies on Li-ion batteries, the cells were positioned vertically in the bore of the magnet, with parallel electrodes on either side of the electrolyte, aligned perpendicular to the B_0 field. Profiles of the electrolyte in both studies showed lower signal-to-noise ratio close to the metal electrodes, caused by variations in the B_1 field strength and sensitivity in this region, but the effects of this were minimised by normalisation of the profiles. Additionally, slight distortions were observed [44] in the frequency-encoded profiles near the metallic electrodes, caused by susceptibility effects at the metal−electrolyte interface. Pure phase-encoding imaging is less susceptible to these artefacts and, hence, viable data can be collected closer to the metal−electrolyte interface with these measurements [144].

<Figure 14 near here>

Changes in electrode microstructure, and the formation of dendrites, have also been investigated by Jerschow, Grey and co-workers [43], in symmetrical Li-metal bag cells, using 2D and 3D ^{7}Li spin density images and 2D ^{7}Li chemical shift images (CSI). While the formation of microstructural lithium has been observed using other imaging techniques (see [147] and references within), these experiments nicely demonstrate how MRI is able to provide in situ quantitative, spatially-resolved information about the behaviour of the electrode during cycling. The cells used in this study [43] comprised parallel lithium

electrodes, aligned parallel to the B_0 field, separated by a porous glass microfiber separator soaked in the electrolyte (LiPF$_6$ dissolved in a 1:1 ratio mixture of ethyl carbonate:dimethyl carbonate). The metallic lithium was imaged, rather than Li ions in the electrolyte, by selectively exciting the bulk-metal signal, which has a chemical shift approximately 270 ppm away from the signal of Li in the electrolyte. Due to the limited penetration of the B_1 field into metals [142], only the surface of the metal was observed. Prior to charging, only the positive and negative electrodes could be detected in the 2D and 3D spin-density ^{7}Li MR images (Fig. 15 (a)). After charging, the presence of microstructural Li near the negative electrode was also observed, with a corresponding reduction in signal for the positive electrode (Fig. 15 (b)). CSI was able to differentiate between the different Li metal signals, because the chemical shifts for the lithium metal electrodes were > 274 ppm and the chemical shifts for the microstructural lithium were below this. Acquisition times for these experiments were on the order of 20 min for the 2D images and 40 min for the 3D images, though at a reduced spatial resolution compared to the 2D images. The influence of B_1 field homogeneity was investigated, demonstrating the need for careful alignment of the Li electrodes parallel with the B_1 field, to optimise image quality and minimise quantification errors.

<Figure 15 near here>

The development of lithium dendrite formation was further investigated by collecting 1D concentration profiles for ^{7}Li in both the metallic electrodes and electrolyte, thereby enabling a correlation between the growth of microstructural lithium metal and depletion of lithium salt in the electrolyte to be made [141]. By collecting concentration profiles across a 1D symmetrical lithium cell, where the electrodes were aligned perpendicular to the B_0 field, a uniform distribution of lithium was initially observed across the electrolyte and

between the two electrodes, prior to the application of current. After the application of current for > 10 hours, a loss of lithium in the positive electrode and an increase for the negative electrode were observed, along with the establishment of a concentration gradient of lithium in the electrolyte. These features continued to develop as more current was applied, with, eventually, the formation of dendrites on the negative electrode.

In situ MRI studies of lithium batteries containing plastic crystal electrolytes have been undertaken by Forsyth and co-workers, using single point ramped imaging with T_1 enhancement (SPRITE) [145, 148]. Pure-phase encoding imaging methods, such as single point imaging (SPI) and SPRITE, are particularly useful when imaging materials with very short T_2 relaxation times ($\leq$ 1 ms), and hence lend themselves especially to the study of solid electrolytes, such as organic ionic plastic crystals (OIPCs). These solid-state MRI experiments [149] have shown a large variation in the microcrystallite alignment of OIPCs, which influences ion transport properties, depending on their thermal history. SPRITE experiments on OIPCs in solid-state lithium cells have shown that lithium ion transfer during the discharge of the anode result in partial liquefaction of the OIPC matrix at the metal interface. This liquid component was found to further enhance the ion transport across the interface and to improve the overall battery performance. In this study, the concentration of lithium in the electrolyte was correlated with the T_2* contrast of the ^{1}H MRI signal from the phosphonium cations in the electrolyte. [7]Li SPRITE has also been used to visualise lithium metal, and by combining these measurements with sectoral fast spin echo imaging sequences, it has been demonstrated both liquid and solid lithium battery components can be imaged in 3D [145].

9.3 Supercapacitors

NMR spectroscopy has proved particularly useful for probing processes in electrochemical double-layer capacitor (EDLC) cells, enabling investigation of charging mechanisms and the interactions and distribution of anions and cations, in situ and in real time [130, 150-152]. However, in order to be able to distinguish between processes occurring at the two electrodes it was necessary to modify the cells, and to perform separate NMR experiments with only one electrode in the RF coil at a time. However, this is time-consuming and cell modification may also have an impact on the performance and behaviour of the cell. By using MRI, it is possible to monitor, in situ, changes at both electrodes simultaneously, within an unmodified working EDLC cell. In a recent study by Jerschow, Grey and co-workers [153], a series of MR images was acquired, during electrochemical cycling, which enabled the distributions of ions to be visualised in the cell as a function of applied voltage. The EDLC cell comprised activated carbon electrodes with an organic NEt_4^+/BF_4^- electrolyte solvated by (deuterated) acetonitrile. Using ^{1}H MRI, the distribution and concentration of the NEt_4^+ cations were monitored, and [11]B MRI allowed selective visualisation of the BF_4^- anions. The chemical shifts for both the ^{1}H and ^{11}B NMR signals were found to be sensitive to the environment of the ions, with three distinct environments observed: free electrolyte in the separator; a strongly adsorbed (SA) or confined environment close to the carbon surface; and a weakly adsorbed (WA) environment either outside the pores or inside larger pores within the carbon electrode. 1D chemical shift images supported these assignments of the NMR peaks, showing that the signals for the SA and WA environments were confined inside the electrodes and the intense, narrow signals associated with free electrolyte in the separator were distributed between the two electrodes (Fig. 16) [153].

<Figure 16 near here>

9.4 Fuel Cells

Another electrochemical energy storage device studied by MRI is the fuel cell [129, 134, 154-161]. A number of studies have investigated the distribution and dynamics of solvent within Nafion polymer membranes and films, which are widely used in fuel cells, as well as ion exchange membranes and actuator devices. In proton-exchange membrane fuel cells (PEMFC), it is important to be able to monitor the distribution of water [157], which influences the performance and longevity of the cell. Wasylishen and co-workers used MRI to map the distribution of water in operating PEMFCs, and found a connection between the water signal intensity and changes in PEMFC operating conditions [158]. Experiments by Codd *et al.* [156] looked at the spatial variation of solvent dynamics within Nafion membranes using T_2 and diffusion imaging. In these polymer electrolyte membranes, T_2 relaxation is predominantly dependent on the mobility of the water molecules and the observed increase in T_2, with increasing methanol mole fraction, was attributed to an increase in the size of channels and ionic domains in the membrane. Diffusion coefficients were also found to increase with increasing methanol concentration, further confirming there was a methanol-induced pore size increase. These measurements allowed spatial mapping of the methanol-water mole fraction and showed that there was significant variability in solvent mobility within the membrane over macroscopic length scales, on the order of 10 mm.

Baker *et al.* [162, 163] have used spin density, T_2 relaxation and diffusion-weighted imaging to study Nafion polymers inside actuator devices. In these studies, they set up an operational electrochemical cell inside the MRI instrument, and imaged the water inside the Nafion film as a function of applied potential. In these systems, T_2 relaxation times, which are sensitive to the strength of the interaction between the water molecules and their immediate environment, were found to increase near the cathode. This behaviour

41

was explained in terms of the electro-induced diffusion of $[Li(H_2O)_x]^+$ species through the Nafion film. More recently, high-temperature polybenzimidazole-based PEMFCs have been investigated in 3D by MRI. These devices have a low water content, and the low mobility of protons within the polybenzimidazole membrane results in short T_2 relaxation times, making it necessary to use Zero-Time Echo (ZTE) MRI experiments, which are designed to image short-T_2 samples [164]. [1]H ZTE images were collected to map the distributions of water and phosphoric acid within the fuel cell, before and during operation, at 80°C.

9.5 Electrochemistry in Flow

Electrochemical cells containing rotating disk electrodes (RDE) are commonly used devices for characterising electrochemical reactions. The rotating disk drags neighbouring fluid across its surface, before centrifugal forces eject it radially, outwards, drawing fresh material on to the electrode surface and, hence, maintaining a constant supply of electroactive species. By inducing convection in the electrolyte, such cells improve mass transport towards the electrode [165]. Thus, knowledge of the flow field, and of mass transfer in the vicinity of the electrode, is critical in the analysis and interpretation of electrochemical data in these cells. Of particular importance in RDEs is the component of flow normal to the electrode, which is dependent on the rotation rate of the disk. While model equations have been developed to describe the flow field in these systems, these equations do not take into account many of the experimental conditions for real RDE cells. Also, the validity of these equations has mostly been tested using computer simulations, and there is currently very limited experimental data available on the flow patterns inside electrochemical cells with RDE configurations. This has recently been addressed by a MRI study visualising the flow field in a model electrochemical cell with a RDE configuration [166]. In this study, velocity maps were acquired (Fig. 17) of the whole cell

as a function of the disk rotating speed and cell configuration, and found to be in good agreement with previous computational fluid dynamics simulations. In these experiments a modified velocity imaging sequence was employed, which placed both of the flow encoding gradients (G_Δ) after the 180˚ RF pulse, to enable a short observation time ($\Delta \lesssim 3$ ms).

<Figure 17 near here>

10. Conclusions

While MRI has been most commonly associated with biomedical imaging and clinical diagnosis, it is also proving invaluable in the fields of engineering and physical science. Its ability to non-invasively probe chemical and physical properties, *in situ,* in real time and in systems not accessible optically, has advanced our understanding of the underlying processes within chemical reactors, heterogeneous chemical processes, spatially-distributed chemical reactions and electrochemical cells. It is able to provide unique information on the coupling of reaction with flow, heterogeneous reaction media, magnetic fields and electrical current. In the last 10-20 years, the variety and range of chemical systems studied by MRI has been expanding at an ever-increasing rate, with the technique continually moving into new areas. This has been encouraged in recent times by the increasing availability of high-resolution MR microimaging apparatus and the rapidly expanding market for bench-top instruments. While bench-top instruments have lower resolution, they are easier to house and maintain, because of the electro- or permanent magnets they are equipped with. Hence, they are increasing the accessibility of the technique to the non-specialist, as well as moving the technique out of the specialist laboratory and putting it into the field. Thus, it is in this area that the next expansion of the field can be expected.

References

[1] F. Susanne, D.S. Smith, A. Codina, Kinetic Understanding Using NMR Reaction Profiling, Org. Process Res. Dev., 16 (2012) 61-64.

[2] T. Blasco, Insights into reaction mechanisms in heterogeneous catalysis revealed by in situ NMR spectroscopy, Chem. Soc. Rev., 39 (2010) 4685-4702.

[3] D.A. Foley, A.L. Dunn, M.T. Zell, Reaction monitoring using online vs tube NMR spectroscopy: seriously different results, Magn. Reson. Chem., 54 (2015) 451-456.

[4] F. Dalitz, M. Cudaj, M. Maiwald, G. Guthausen, Process and reaction monitoring by low-field NMR spectroscopy, Prog. Nucl. Magn. Reson. Spec., 60 (2012) 52-70.

[5] M.M. Britton, Magnetic resonance imaging of chemistry, Chem. Soc. Rev., 39 (2010) 4036-4043.

[6] M.M. Britton, Porous Media Studied by MRI, in: Encyclopedia of Magnetic Resonance, John Wiley & Sons, Ltd, 2011.

[7] A.A. Lysova, I.V. Koptyug, Magnetic resonance imaging methods for in situ studies in heterogeneous catalysis, Chem. Soc. Rev., 39 (2010) 4585-4601.

[8] M.D. Mantle, A.J. Sederman, Dynamic MRI in chemical process and reaction engineering, Prog. Nucl. Magn. Reson. Spec., 43 (2003) 3-60.

[9] S. Stapf, S.-I. Han, NMR Imaging in Chemical Engineering, Wiley-VCH, Weinheim, 2006.

[10] L.F. Gladden, Applications of in situ magnetic resonance techniques in chemical reaction engineering, Topics in Catalysis, 8 (1999) 87-95.

[11] L.F. Gladden, Recent advances in MRI studies of chemical reactors: ultrafast imaging of multiphase flows, Topics in Catalysis, 24 (2003) 19-28.

[12] E.L. Gjersing, S.L. Codd, J.D. Seymour, P.S. Stewart, Magnetic resonance microscopy analysis of advective transport in a biofilm reactor, Biotech. Bioeng., 89 (2005) 822-834.

[13] J.D. Seymour, S.L. Codd, E.L. Gjersing, P.S. Stewart, Magnetic resonance microscopy of biofilm structure and impact on transport in a capillary bioreactor, J. Magn. Reson., 167 (2004) 322-327.

[14] J.D. Seymour, J.P. Gage, S.L. Codd, R. Gerlach, Magnetic resonance microscopy of biofouling induced scale dependent transport in porous media, Adv. Water Resour., 30 (2007) 1408-1420.

[15] V.R. Phoenix, W.M. Holmes, Magnetic resonance imaging of structure, diffusivity, and copper immobilization in a phototrophic biofilm, Appl Environ Microb, 74 (2008) 4934-4943.

[16] D.A.G. von der Schulenburg, B.S. Akpa, L.F. Gladden, M.L. Johns, Non-invasive mass transfer measurements in complex biofilm-coated structures, Biotech. Bioeng., 101 (2008) 602-608.

[17] R. Nigmatullin, M. Bencsik, F. Gao, Influence of polymerisation conditions on the properties of polymer/clay nanocomposite hydrogels, Soft Matter, 10 (2014) 2035-2046.

[18] B. Manz, J. Masere, J.A. Pojman, F. Volke, Magnetic resonance imaging of spiral patterns in crosslinked polymer gels produced via frontal polymerization, J. Polym. Sci. Pol. Chem., 39 (2001) 1075-1080.

[19] T.G. Nunes, F.C.P. Garcia, R. Osorio, R. Carvalho, M. Toledano, Polymerization efficacy of simplified adhesive systems studied by NMR and MRI techniques, Dent. Mater., 22 (2006) 963-972.

[20] R.L. Armstrong, A. Tzalmona, M. Menzinger, A. Cross, C. Lemaire, Imaging the Dynamics of Chemical Waves: the Belousov-Zhabotinsky reaction, in: B. Blümich, W. Kuhn (Eds.) Magnetic Resonance Microscopy: methods and application in materials science, agriculture and biomedicine, VCH, Weinheim, 1992.

[21] A.F. Taylor, M.M. Britton, Magnetic resonance imaging of chemical waves in porous media, Chaos: An Interdisciplinary Journal of Nonlinear Science, 16 (2006) 037103.

[22] M.M. Britton, Magnetic Resonance Imaging of Electrochemical Cells Containing Bulk Metal, Chemphyschem, 15 (2014) 1731-1736.

[23] B.S. Akpa, M.D. Mantle, A.J. Sederman, L.F. Gladden, In situ C-13 DEPT-MRI as a tool to spatially resolve chemical conversion and selectivity of a heterogeneous catalytic reaction occurring in a fixed-bed reactor, Chem. Comm., (2005) 2741-2743.

[24] E.H.L. Yuen, A.J. Sederman, L.F. Gladden, In situ magnetic resonance visualisation of the spatial variation of catalytic conversion within a fixed-bed reactor, App. Cat. A, 232 (2002) 29-38.

[25] I.R. Epstein, J.A. Pojman, An Introduction to Nonlinear Chemical Dynamics, Oxford University Press, Oxford, 1998.

[26] A.N. Zaikin, A. M.Zhabotinsky, Concentration Wave Propagation in 2-Dimensional Liquid-Phase Self-Oscillating System, Nature, 225 (1970) 535-537 .

[27] J. Novak, B.W. Thompson, M.C.T. Wilson, A.F. Taylor, M.M. Britton, Low frequency temperature forcing of chemical oscillations, Phys. Chem. Chem. Phys., 13 (2011) 12321–12327.

[28] M.M. Britton, A.J. Sederman, A.F. Taylor, S.K. Scott, L.F. Gladden, Magnetic resonance imaging of flow-distributed oscillations, J. Phys. Chem. A, 109 (2005) 8306-8313.

[29] A. Vallatos, R. Evans, B.W. Thompson, A.F. Taylor, M.M. Britton, Chemical patterns in translating vortices: Inter- and intra-cellular mixing effects, Chaos: An Interdisciplinary Journal of Nonlinear Science, 23 (2013) 023115.

[30] B.W. Thompson, J. Novak, M.C.T. Wilson, M.M. Britton, A.F. Taylor, Inward propagating chemical waves in Taylor vortices, Phys. Rev. E, 81 (2010) 047101.

[31] M. Kaern, M. Menzinger, Flow-distributed oscillations: Stationary chemical waves in a reacting flow, Physical Review E, 60 (1999) R3471-R3474.

[32] A.B. Rovinsky, M. Menzinger, Chemical-Instability Induced by a Differential Flow, Phys Rev Lett, 69 (1992) 1193-1196.

[33] P.T. Callaghan, Principles of Nuclear Magnetic Resonance Microscopy, Oxford University Press, Oxford, 1991.

[34] B. Blümich, NMR imaging of materials, Oxford University Press, Oxford, 2000.

[35] P. Mansfield, P.K. Grannell, NMR Diffraction in Solids, J Phys C Solid State, 6 (1973) L422-L426.

[36] P. Mansfield, Multi-planar image-formation using NMR spin echoes J Phys C Solid State, 10 (1977) L55-L58.

[37] J. Hennig, A. Naureth, H. Friedburg, RARE imaging: A fast imaging method for clinical MR, Magn. Reson. Med., 3 (1986) 823-833.

[38] A. Haase, J. Frahm, D. Matthaei, W. Hanicke, K.D. Merboldt, Flash imaging - rapid NMR imaging using low flip-angle pulses, J. Magn. Reson., 67 (1986) 258-266.

[39] R.E. Mewis, Developments and advances concerning the hyperpolarisation technique SABRE, Magn. Reson. Chem., 53 (2015) 789-800.

[40] M. Roth, A. Koch, P. Kindervater, J. Bargon, H.W. Spiess, K. Munnemann, C-13 hyperpolarization of a barbituric acid derivative via parahydrogen induced polarization, J. Magn. Reson., 204 (2010) 50-55.

[41] E. Moser, F. Stahlberg, M.E. Ladd, S. Trattnig, 7-T MR-from research to clinical applications?, NMR Biomed., 25 (2012) 695-716.

[42] P.S. Hsieh, R.S. Balaban, P-31 Imaging of in vivo creatine-kinase reaction-rates J. Magn. Reson., 74 (1987) 574-579.

[43] S. Chandrashekar, N.M. Trease, H.J. Chang, L.S. Du, C.P. Grey, A. Jerschow, Li-7 MRI of Li batteries reveals location of microstructural lithium, Nature Materials, 11 (2012) 311-315.

[44] M. Klett, M. Giesecke, A. Nyman, F. Hallberg, R.W. Lindstrom, G. Lindbergh, I. Furo, Quantifying Mass Transport during Polarization in a Li Ion Battery Electrolyte by in Situ Li-7 NMR Imaging, J. Am. Chem. Soc., 134 (2012) 14654-14657.

[45] U. Eliav, G. Navon, Sodium NMR/MRI for anisotropic systems, NMR Biomed., 29 (2016) 144-152.

[46] G.E. Pavlovskaya, T. Meersmann, Spatial Mapping of Flow-Induced Molecular Alignment in a Noncrystalline Biopolymer Fluid Using Double Quantum Filtered (DQF) Na-23 MRI, Journal of Physical Chemistry Letters, 5 (2014) 2632-2636.

[47] R.J. Cormier, P.T. Callaghan, Molecular weight dependence of segmental alignment in a sheared polymer melt: A deuterium nuclear magnetic resonance investigation, Journal of Chemical Physics, 116 (2002) 10020-10029.

[48] C. Lepper, P.J.B. Edwards, E. Schuster, J.R. Brown, R. Dykstra, P.T. Callaghan, M.A.K. Williams, Rheo-NMR studies of the behavior of a nematic liquid crystal in a low-shear-rate regime: The transition from director alignment to reorientation, Phys. Rev. E, 82 (2010) 041712.

[49] J. Kaufmann, W. Studer, J. Link, K. Schenker, Study of water suction of concrete with magnetic resonance imaging methods, Mag. Concr. Res., 49 (1997) 157-165.

[50] I.V. Koptyug, A.V. Khomichev, A.A. Lysova, R.Z. Sagdeev, Spatially resolved NMR thermometry of an operating fixed-bed catalytic reactor, J. Am. Chem. Soc., 130 (2008) 10452-10453.

[51] M.H. Sankey, D.J. Holland, A.J. Sederman, L.F. Gladden, Magnetic resonance velocity imaging of liquid and gas two-phase flow in packed beds, J. Magn. Reson., 196 (2009) 142-148.

[52] R.E. Gerald, A.O. Krasavin, R.E. Botto, A Selective-Echo Method for Chemical-Shift Imaging of Two-Component Systems, J. Magn. Reson. A, 123 (1996) 201-206.

[53] R. Kimmich, G. Schnur, D. Hoepfel, D. Ratzel, Volume-Selective Multipulse Spin-Echo Spectroscopy and Selective Suppression of Spectral-Lines, Phys Med Biol, 32 (1987) 1335-1343.

[54] R. Kimmich, D. Hoepfel, Volume-Selective Multipulse Spin-Echo Spectroscopy, J. Magn. Reson., 72 (1987) 379-384.

[55] L.F. Gladden, M.D. Mantle, A.J. Sederman, E.H.L. Yuen, Magnetic resonance imaging of single- and two-phase flow in fixed-bed reactors, App. Magn. Reson., 22 (2002) 201-212.

[56] R.K. Harris, Nuclear Magnetic Resonance Spectroscopy, Longman, Harlow, 1991.

[57] M.H. Levitt, Spin dynamics, Wiley, Chichester, 2002.

[58] V.I. Bakjmutov, Practical NMR relaxation for chemists, Wiley, Chichester, 2004.

[59] A. Kaspar, D. Bilecen, K. Scheffler, J. Seelig, Aluminum-27 nuclear magnetic resonance spectroscopy and imaging of the human gastric lumen, Magn. Reson. Med., 36 (1996) 177-182.

[60] R.B. Lauffer, Paramagnetic Metal Complexes as Water Proton Relaxation Agetns for NMR Imaging: Theory and Design., Chem. Rev., 87 (1987) 901-907.

[61] H.G. Hertz, Microdynamic behaviour of liquids as studied by NMR relaxation times., Prog. Nucl. Magn. Reson. Spec., 3 (1967) 159-230.

[62] J.M. Bray, A.J. Davenport, K.S. Ryder, M.M. Britton, Quantitative, In Situ Visualization of Metal-Ion Dissolution and Transport Using [1]H Magnetic Resonance Imaging, Angew. Chem. Int. Ed., 55 (2016) 9394-9397.

[63] M.M. Britton, Spatial Quantification of Mn^{2+} and Mn^{3+} Concentrations in the Mn-Catalyzed 1,4-Cyclohexanedione/Acid/Bromate Reaction Using Magnetic Resonance Imaging, J. Phys. Chem. A, 110 (2006) 2579-2582.

[64] R. Evans, C.R. Timmel, P.J. Hore, M.M. Britton, Magnetic resonance imaging of a magnetic field-dependent chemical wave, Chem. Phys. Lett., 397 (2004) 67-72.

[65] M.M. Britton, C.R. Timmel, Magnetic Field Control of Chemical Waves, in: S.L. Codd, J.D. Seymour (Eds.) Magnetic Resonance Microscopy: Spatially Resolved NMR Techniques and Applications, Wiley-VCH, Weinheim, 2009, pp. 383-398.

[66] R.B. Lauffer, Paramagnetic Metal Complexes as Water Proton Relaxation Agents for NMR Imaging: Theory and Design., Chem. Rev., 87 (1987) 901-907.

[67] P. Caravan, C.T. Farrar, L. Frullano, R. Uppal, Influence of molecular parameters and increasing magnetic field strength on relaxivity of gadolinium- and manganese-based T(1) contrast agents, Contrast Media Mol I, 4 (2009) 89-100.

[68] M.M. Britton, Nuclear magnetic resonance studies of the 1,4-cyclohexanedione-bromate-acid oscillatory system, J. Phys. Chem. A, 107 (2003) 5033-5041.

[69] R. Evans, K.B. Henbest, M.A. Hayward, M.M. Britton, K. Maeda, C.R. Timmel, SQUID magnetometry as a tool for following a clock reaction in solution, Dalton Trans., (2009) 2467-2469.

[70] C. Deverell, NMR Studies of Electrolyte Solutions, Prog. Nucl. Magn. Reson. Spec., 4 (1969) 235-334.

[71] H.E.L. Rose, M.M. Britton, Magnetic resonance imaging of reaction-driven viscous fingering in a packed bed, Microporous Mesoporous Mat., 178 (2013) 64-68.

[72] M.M. Britton, R.G. Graham, K.J. Packer, NMR relaxation and pulsed field gradient study of alginate bead porous media, J. Magn. Reson., 169 (2004) 203-214.

[73] L. Buljubasich, B. Blumich, S. Stapf, Quantification of H_2O_2 concentrations in aqueous solutions by means of combined NMR and pH measurements, Phys. Chem. Chem. Phys., 12 (2010) 13166-13173.

[74] N.A. Halliday, A.C. Peet, M.M. Britton, Detection of pH in Microemulsions, without a Probe Molecule, Using Magnetic Resonance, J. Phys. Chem. B, 114 (2010) 13745–13751.

[75] S. Aime, R. Nano, M. Grandi, A New Class of Contrast Agents for Magnetic-Resonance Imaging Based on Selective Reduction of Water-T2 by Chemical-Exchange, Invest. Radiol., 23 (1988) S267-S270.

[76] E.W. Mcfarland, L.J. Neuringer, M.J. Kushmerick, Chemical-Exchange Magnetic-Resonance Imaging (Chemi), Magn. Reson. Imag., 6 (1988) 507-515.

[77] S. Aime, L. Calabi, L. Biondi, M. De Miranda, S. Ghelli, L. Paleari, C. Rebaudengo, E. Terreno, Iopamidol: Exploring the potential use of a well-established X-ray contrast agent for MRI, Magn. Reson. Med., 53 (2005) 830-834.

[78] A.D. Sherry, M. Woods, Chemical Exchange Saturation Transfer Contrast Agents for Magnetic Resonance Imaging, Annual Review of Biomedical Engineering, 10 (2008) 391-411.

[79] L. Schroder, T.J. Lowery, C. Hilty, D.E. Wemmer, A. Pines, Molecular imaging using a targeted magnetic resonance hyperpolarized biosensor, Science, 314 (2006) 446-449.

[80] G. Liu, X. Song, K.W.Y. Chan, M.T. McMahon, Nuts and Bolts of CEST MR imaging, NMR Biomed., 26 (2013) 810-828.

[81] P.T. Callaghan, Translational Dynamics & Magnetic Resonance: Principles of Pulsed Gradient Spin Echo NMR, Oxford University Press: Oxford, 2011.

[82] W.S. Price, NMR Studies of Translational Motion, Cambridge University Press, Cambridge, 2009.

[83] E.O. Stejskal, J.E. Tanner, Spin Diffusion Measurements: Spin Echoes in the Presence of a Time-Dependent Field Gradient, J. Chem. Phys., 42 (1965) 288-292.

[84] A.J. Sederman, L.F. Gladden, Magnetic resonance visualisation of single- and two-phase flow in porous media, Magn. Reson. Imag., 19 (2001) 339-343.

[85] A. Vallatos, R.M. Kirsch, R.A. Williams, R.B. Hammond, X. Jia, U. Bröckel, M.M. Britton, Probing Composition and Molecular Mobility in Thin Spherical Films Using Nuclear Magnetic Resonance Measurements of Diffusion, Industrial & Engineering Chemistry Research, 54 (2015) 6825-6830.

[86] M.M. Britton, P.T. Callaghan, Shear banding instability in wormlike micellar solutions, European Physical Journal B, 7 (1999) 237-249.

[87] Y. Gao, A.R. Cross, R.L. Armstrong, Magnetic resonace imaging of ruthenium-, cerium-, and ferroin-catalyzed Belousov-Zhabotinsky reactions, Journal of Physical Chemistry, 100 (1996) 10159-10164.

[88] A. Tzalmona, R.L. Armstrong, M. Menzinger, A. Cross, C. Lemaire, Detection of chemical waves by magnetic resonance imaging, Chemical Physics Letters, 174 (1990) 199.

[89] A.F. Taylor, M.M. Britton, Magnetic resonance imaging of chemical waves in porous media, Chaos, 16 (2006) 037103.

[90] D.A.G. von der Schulenburg, D.J. Holland, M. Paterson-Beedle, L.E. Macaskie, L.F. Gladden, M.L. Johns, Spatially resolved quantification of metal ion concentration in a biofilm-mediated ion exchanger, Biotech. Bioeng., 99 (2008) 821-829.

[91] E. Boga, S. Kádár, G. Peintler, I. Nagypál, Effect of magnetic fields on a propagating reaction front, Nature, 347 (1990) 749-751.

[92] R. Evans, C.R. Timmel, P.J. Hore, M.M. Britton, Magnetic Resonance Imaging of the Manipulation of a Chemical Wave Using an Inhomogeneous Magnetic Field, J. Am. Chem. Soc., 128 (2006) 7309-7314.

[93] J.D. Seymour, B. Manz, P.T. Callaghan, Pulsed gradient spin echo nuclear magnetic resonance measurements of hydrodynamic instabilities with coherent structure: Taylor vortices, Phys Fluids, 11 (1999) 1104-1113.

[94] A. Vallatos, M.C.T. Wilson, A.F. Taylor, M.M. Britton, Characterising stationary and translating vortex flow using magnetic resonance, Europhys. Lett., 99 (2012) 68001.

[95] J. Novak, Visualisation of Chemistry in Flow, PhD thesis, University of Birmingham, 2010.

[96] M.M. Resende, P.W. Tardioli, V.M. Fernandez, A.L.O. Ferreira, R.L.C. Giordano, R.C. Giordano, Distribution of suspended particles in a Taylor-Poiseuille vortex flow reactor, Chemical Engineering Science, 56 (2001) 755-761.

[97] L.J. Forney, J.A. Pierson, Optimum photolysis in Taylor-Couette flow, AIChE J., 49 (2003) 727-733.

[98] B. Haut, H. Ben Amor, L. Coulon, A. Jacquet, V. Halloin, Hydrodynamics and mass transfer in a Couette-Taylor bioreactor for the culture of animal cells, Chemical Engineering Science, 58 (2003) 777-784.

[99] B. Judat, A. Racina, M. Kind, Macro- and micromixing in a Taylor-Couette reactor with axial flow and their influence on the precipitation of barium sulfate, Chemical Engineering & Technology, 27 (2004) 287-292.

[100] J. Wolinski, S. Wronski, Interfacial polycondensation of polyarylate in Taylor-Couette-Reactor, Chemical Engineering and Processing, 48 (2009) 1061-1071.

[101] A.J. Sederman, M.L. Johns, P. Alexander, L.F. Gladden, Structure-flow correlations in packed beds, Chemical Engineering Science, 53 (1998) 2117-2128.

[102] D. Weber, D.J. Holland, L.F. Gladden, Spatially and chemically resolved measurement of intra- and inter-particle molecular diffusion in a fixed-bed reactor, Applied Catalysis a-General, 392 (2011) 192-198.

[103] B. Newling, Gas flow measurements by NMR, Prog. Nucl. Magn. Reson. Spec., 52 (2008) 31-48.

[104] M.S. Albert, G.D. Cates, B. Driehuys, W. Happer, B. Saam, C.S. Springer, A. Wishnia, Biological Magnetic-Resonance-Imaging Using Laser Polarized Xe-129, Nature, 370 (1994) 199-201.

[105] N.N. Jarenwattananon, S. Gloggler, T. Otto, A. Melkonian, W. Morris, S.R. Burt, O.M. Yaghi, L.S. Bouchard, Thermal maps of gases in heterogeneous reactions, Nature, 502 (2013) 537-540.

[106] I.V. Koptyug, S.A. Altobelli, E. Fukushima, A.V. Matveev, R.Z. Sagdeev, Thermally polarized H-1 NMR microimaging studies of liquid and gas flow in monolithic catalysts, J. Magn. Reson., 147 (2000) 36-42.

[107] D.O. Kuethe, A. Caprihan, E. Fukushima, R.A. Waggoner, Imaging lungs using inert fluorinated gases, Magn. Reson. Med., 39 (1998) 85-88.

[108] B. Newling, C.C. Poirier, Y. Zhi, J.A. Rioux, A.J. Coristine, D. Roach, B.J. Balcom, Velocity imaging of highly turbulent gas flow, Phys Rev Lett, 93 (2004) 154503.

[109] S.D. Beyea, S.A. Altobelli, L.A. Mondy, Chemically selective NMR imaging of a 3-component (solid-solid-liquid) sedimenting system, J. Magn. Reson., 161 (2003) 198-203.

[110] L.-S. Bouchard, S.R. Burt, M.S. Anwar, K.V. Kovtunov, I.V. Koptyug, A. Pines, NMR imaging of catalytic hydrogenation in microreactors with the use of para-hydrogen, Science, 319 (2008) 442-445.

[111] L.F. Gladden, F.J.R. Abegão, C.P. Dunckley, D.J. Holland, M.H. Sankey, A.J. Sederman, MRI: Operando measurements of temperature, hydrodynamics and local reaction rate in a heterogeneous catalytic reactor, Catalysis Today, 155 (2010) 157-163.

[112] P. Parasoglou, D. Malioutov, A.J. Sederman, J. Rasburn, H. Powell, L.F. Gladden, A. Blake, M.L. Johns, Quantitative single point imaging with compressed sensing, J. Magn. Reson., 201 (2009) 72-80.

[113] D.J. Holland, D.M. Malioutov, A. Blake, A.J. Sederman, L.F. Gladden, Reducing data acquisition times in phase-encoded velocity imaging using compressed sensing, J. Magn. Reson., 203 (2010) 236-246.

[114] E. von Harbou, H.T. Fabich, M. Benning, A.B. Tayler, A.J. Sederman, L.F. Gladden, D.J. Holland, Quantitative mapping of chemical compositions with MRI using compressed sensing, J. Magn. Reson., 261 (2015) 27-37.

[115] T. Kampf, A. Fischer, T.C. Basse-Lusebrink, G. Ladewig, F. Breuer, G. Stoll, P.M. Jakob, W.R. Bauer, Application of compressed sensing to in vivo 3D F-19 CSI, J. Magn. Reson., 207 (2010) 262-273.

[116] S. Hu, M. Lustig, A.P. Chen, J. Crane, A. Kerr, D.A.C. Kelley, R. Hurd, J. Kurhanewicz, S.J. Nelson, J.M. Pauly, D.B. Vigneron, Compressed sensing for resolution enhancement of hyperpolarized C-13 flyback 3D-MRSI, J. Magn. Reson., 192 (2008) 258-264.

[117] S. Hu, M. Lustig, A. Balakrishnan, P.E.Z. Larson, R. Bok, J. Kurhanewicz, S.J. Nelson, A. Goga, J.M. Pauly, D.B. Vigneron, 3D Compressed Sensing for Highly Accelerated Hyperpolarized C-13 MRSI With In Vivo Applications to Transgenic Mouse Models of Cancer, Magn. Reson. Med., 63 (2010) 312-321.

[118] A. De Wit, Fingering of Chemical Fronts in Porous Media, Phys. Rev. Lett., 87 (2001) 054502.

[119] J. Fernandez, G.M. Homsy, Viscous fingering with chemical reaction: effect of in-situ production of surfactants, J Fluid Mech, 480 (2003) 267-281.

[120] E.S. Davies, T.A. Carpenter, L.D. Hall, C. Hall, NMR imaging of fractal fingering in Hele-Shaw cells, AIChE J., 39 (1993) 510-512.

[121] E.J. Fernandez, C.A. Grotegut, G.W. Braun, K.J. Kirschner, J.R. Staudaher, M.L. Dickson, V.L. Fernandez, The Effects Of Permeability Heterogeneity On Miscible Viscous Fingering - A 3-Dimensional Magnetic-Resonance-Imaging Analysis, Phys. Fluids, 7 (1995) 468-477.

[122] T. Podgorski, M.C. Sostarecz, S. Zorman, A. Belmonte, Fingering instabilities of a reactive micellar interface, Phys. Rev. E, 76 (2007) 016202.

[123] I.V. Koptyug, D.R. Sagdeev, E. Gerkema, H. Van As, R.Z. Sagdeev, Solid-state Al-27 MRI and NMR thermometry for catalytic applications with conventional (liquids) MRI instrumentation and techniques, J. Magn. Reson., 175 (2005) 21-29.

[124] V.V. Zhivonitko, I.V. Koptyug, R.Z. Sagdeev, Temperature changes visualization during chemical wave propagation, J. Phys. Chem. A, 111 (2007) 4122-4124.

[125] J.P. Hindmarsh, C. Buckley, A.B. Russell, X.D. Chen, L.F. Gladden, D.I. Wilson, M.L. Johns, Imaging droplet freezing using MRI, Chemical Engineering Science, 59 (2004) 2113-2122.

[126] R. Mahdjoub, P. Chouvenc, M.J. Seurin, J. Andrieu, A. Briguet, Sucrose solution freezing studied by magnetic resonance imaging, Carbohyd Res, 341 (2006) 492-498.

[127] K. Beravs, A. Demsar, F. Demsar, Magnetic resonance current density imaging of chemical processes and reactions, J. Magn. Reson., 137 (1999) 253-257.

[128] U. Mikac, A. Demsar, F. Demsar, I. Sersa, A study of tablet dissolution by magnetic resonance electric current density imaging, J. Magn. Reson., 185 (2007) 103-109.

[129] F. Blanc, M. Leskes, C.P. Grey, In Situ Solid-State NMR Spectroscopy of Electrochemical Cells: Batteries, Supercapacitors, and Fuel Cells, Acc. Chem. Res., 46 (2013) 1952-1963.

[130] A.C. Forse, C. Merlet, J.M. Griffin, C.P. Grey, New Perspectives on the Charging Mechanisms of Supercapacitors, J. Am. Chem. Soc., 138 (2016) 5731-5744.

[131] J.M. Griffin, A.C. Forse, C.P. Grey, Solid-state NMR studies of supercapacitors, Solid State Nucl. Magn. Reson., 74-75 (2016) 16-35.

[132] C.P. Grey, N. Dupré, NMR Studies of Cathode Materials for Lithium-Ion Rechargeable Batteries, Chem. Rev., 104 (2004) 4493-4512.

[133] O.H. Han, Nuclear magnetic resonance investigations on electrochemical reactions of low temperature fuel cells operating in acidic conditions, Prog. Nucl. Magn. Reson. Spec., 72 (2013) 1-41.

[134] O.H. Han, K.S. Han, C.W. Shin, J. Lee, S.-S. Kim, M.S. Um, H.-I. Joh, S.-K. Kim, H.Y. Ha, Observation of Methanol Behavior in Fuel Cells In Situ by NMR Spectroscopy, Angew. Chem. Int. Ed., 51 (2012) 3842-3845.

[135] R.E. Gerald, R.J. Klingler, G. Sandi, C.S. Johnson, L.G. Scanlon, J.W. Rathke, Li-7 NMR study of intercalated lithium in curved carbon lattices, J. Power Sources, 89 (2000) 237-243.

[136] R.E. Gerald, J. Sanchez, C.S. Johnson, R.J. Klingler, J.W. Rathke, In situ nuclear magnetic resonance investigations of lithium ions in carbon electrode materials using a novel detector, J Phys-Condens Mat, 13 (2001) 8269-8285.

[137] J.W. Rathke, R.J. Klingler, R.E. Gerald, K.W. Kramarz, K. Woelk, Toroids in NMR spectroscopy, Prog. Nucl. Magn. Reson. Spec., 30 (1997) 209-253.

[138] K.I. Momot, N. Binesh, O. Kohlmann, C.S. Johnson, Toroid cavity detectors for high-resolution NMR spectroscopy and rotating frame imaging: Capabilities and limitations, J. Magn. Reson., 142 (2000) 348-357.

[139] A.J. Davenport, M. Forsyth, M.M. Britton, Visualisation of chemical processes during corrosion of zinc using magnetic resonance imaging, Electrochem. Comm., 12 (2010) 44-47.

[140] M.M. Britton, P.M. Bayley, P.C. Howlett, A.J. Davenport, M. Forsyth, In Situ, Real-Time Visualization of Electrochemistry Using Magnetic Resonance Imaging, J. Phys. Chem. Lett. 4 (2013) 3019-3023.

[141] H.J. Chang, A.J. Ilott, N.M. Trease, M. Mohammadi, A. Jerschow, C.P. Grey, Correlating Microstructural Lithium Metal Growth with Electrolyte Salt Depletion in Lithium Batteries Using Li-7 MRI, J. Am. Chem. Soc., 137 (2015) 15209-15216.

[142] A.J. Ilott, S. Chandrashekar, A. Kloeckner, H.J. Chang, N.M. Trease, C.P. Grey, L. Greengard, A. Jerschow, Visualizing skin effects in conductors with MRI: Li-7 MRI experiments and calculations, J. Magn. Reson., 245 (2014) 143-149.

[143] M. Giesecke, S.V. Dvinskikh, I. Furo, Constant-time chemical-shift selective imaging, J. Magn. Reson., 226 (2013) 19-21.

[144] S.A. Krachkovskiy, J.D. Bazak, P. Werhun, B.J. Balcom, I.C. Halalay, G.R. Goward, Visualization of Steady-State Ionic Concentration Profiles Formed in Electrolytes during Li-Ion Battery Operation and Determination of Mass-Transport Properties by in Situ Magnetic Resonance Imaging, J. Am. Chem. Soc., 138 (2016) 7992-7999.

[145] K. Romanenko, M. Forsyth, L.A. O'Dell, New opportunities for quantitative and time efficient 3D MRI of liquid and solid electrochemical cell components: Sectoral Fast Spin Echo and SPRITE, J. Magn. Reson., 248 (2014) 96-104.

[146] B. Winther-Jensen, M. Gaadingwe, D.R. Macfarlane, M. Forsyth, Control of magnesium interfacial reactions in aqueous electrolytes towards a biocompatible battery, Electrochimica Acta, 53 (2008) 5881-5884.

[147] H.J. Chang, N.M. Trease, A.J. Ilott, D.L. Zeng, L.S. Du, A. Jerschow, C.P. Grey, Investigating Li Microstructure Formation on Li Anodes for Lithium Batteries by in Situ Li-6/Li-7 NMR and SEM, J. Phys. Chem. C, 119 (2015) 16443-16451.

[148] K. Romanenko, L.Y. Jin, P. Howlett, M. Forsyth, In Situ MRI of Operating Solid-State Lithium Metal Cells Based on Ionic Plastic Crystal Electrolytes, Chem. Mat., 28 (2016) 2844-2851.

[149] K. Romanenko, L.Y. Jin, L.A. Madsen, J.M. Pringle, L.A. O'Dell, M. Forsyth, Anisotropic MRI Contrast Reveals Enhanced Ionic Transport in Plastic Crystals, J. Am. Chem. Soc., 136 (2014) 15638-15645.

[150] J.M. Griffin, A.C. Forse, W.Y. Tsai, P.L. Taberna, P. Simon, C.P. Grey, In situ NMR and electrochemical quartz crystal microbalance techniques reveal the structure of the electrical double layer in supercapacitors, Nature Materials, 14 (2015) 812-819.

[151] H. Wang, A.C. Forse, J.M. Griffin, N.M. Trease, L. Trognko, P.L. Taberna, P. Simon, C.P. Grey, In Situ NMR Spectroscopy of Supercapacitors: Insight into the Charge Storage Mechanism, J. Am. Chem. Soc., 135 (2013) 18968-18980.

[152] H. Wang, T.K.J. Koster, N.M. Trease, J. Segalini, P.L. Taberna, P. Simon, Y. Gogotsi, C.P. Grey, Real-Time NMR Studies of Electrochemical Double-Layer Capacitors, J. Am. Chem. Soc., 133 (2011) 19270-19273.

[153] A.J. Ilott, N.M. Trease, C.P. Grey, A. Jerschow, Multinuclear in situ magnetic resonance imaging of electrochemical double-layer capacitors, Nat Commun, 5 (2014) 4536.

[154] S. Tsushima, S. Hirai, Magnetic Resonance Imaging of Water in Operating Polymer Electrolyte Membrane Fuel Cells, Fuel Cells, 9 (2009) 506-517.

[155] L.M. Yan, Y.D. Hu, X.M. Zhang, B.H. Yue, Applications of NMR Techniques in the Development and Operation of Proton Exchange Membrane Fuel Cells, in: G.A. Webb (Ed.) Annual Reports on NMR Spectroscopy, Vol 88, 2016, pp. 149-213.

[156] S.L. Codd, D.T. Howe, J.D. Seymour, E.H. Werre, S.C. Busse, E.S. Peterson, Magnetic resonance Microscopy of heterogeneity in polymer electrolyte membranes, App. Magn. Reson., 32 (2007) 13-24.

[157] K.W. Feindel, S.H. Bergens, R.E. Wasylishen, The use of H-1 NMR microscopy to study proton-exchange membrane fuel cells, Chemphyschem, 7 (2006) 67-75.

[158] K.W. Feindel, S.H. Bergens, R.E. Wasylishen, The influence of membrane electrode assembly water content on the performance of a polymer electrolyte membrane fuel cell as investigated by H-1 NMR microscopy, Phys. Chem. Chem. Phys., 9 (2007) 1850-1857.

[159] K.W. Feindel, L.P.A. LaRocque, D. Starke, S.H. Bergens, R.E. Wasylishen, In situ observations of water production and distribution in an operating H-2/O-2 PEM fuel cell assembly using H-1 NMR microscopy, J. Am. Chem. Soc., 126 (2004) 11436-11437.

[160] Z. Zhang, J. Martin, J. Wu, H. Wang, K. Promislow, B.J. Balcom, Magnetic resonance imaging of water content across the Nafion membrane in an operational PEM fuel cell, J. Magn. Reson., 193 (2008) 259-266.

[161] A.S. Cattaneo, D.C. Villa, S. Angioni, C. Ferrara, R. Melzi, E. Quartarone, P. Mustarelli, Operando electrochemical NMR microscopy of polymer fuel cells, Ener. Environ. Sci., 8 (2015) 2383-2388.

[162] R.T. Baker, L. Naji, K. Lochhead, J.A. Chudek, In situ magnetic resonance imaging of electrically-induced water diffusion in a Nafion ionic polymer film, Chem. Commun., (2003) 962-963.

[163] L. Naji, J.A. Chudek, R.T. Baker, Time-Resolved Mapping of Water Diffusion Coefficients in a Working Soft Actuator Device, J. Phys. Chem. B, 112 (2008) 9761-9768.

[164] M. Weiger, K.P. Pruessmann, MRI with Zero Echo Time, in: eMagRes, John Wiley & Sons, Ltd, 2007.

[165] A.C. Fisher, Electrode Dynamics, Oxford University Press, Oxford, 2003.

[166] M. Carpinella, M.I. Velasco, E.V. Silletta, J.M. Ovejero, S.A. Dassie, R.H. Acosta, Determination of flow patterns in a rotating disk electrode configuration by MRI, J Electroanal Chem, 750 (2015) 100-106.

51

Figure Captions

Figure 1. A time series of MR images of traveling chemical waves in the Mn-catalyzed BZ reaction, taken from the centre of a packed-bed reactor. Waves are formed both inside a packed bed of 1 mm glass particles and above in the liquid phase. Images are shown at intervals of 16 s. Reprinted with permission from reference [28] Copyright 2006 American Chemical Society.

Figure 2. (a) T_2-weighted RARE image of chemical waves in the Mn-catalyzed 1,4-cyclohexanedione/acid/bromate reaction, (b) T_2 relaxation time map and (c) Mn^{2+} and Mn^{3+} concentration maps. The T_2 and concentration maps were produced from the image in (a). Reprinted with permission from reference [63]. Copyright 2006 American Chemical Society.

Figure 3. MR images of a travelling chemical front formed in the reaction of $Co(II)EDTA^{2-}$ with H_2O_2. The image in (a) was taken 20 s after front initiation. Following image (a), a magnetic field gradient ($\boldsymbol{B_z}$) was applied between imaging experiments. For the images shown in (b) and (c) the applied gradients were in the -y direction. Following image (c) the direction of the gradient was switched to +y. The arrows indicate the direction in which the magnetic field increased during the gradient trains which were applied prior to acquiring the images. Adapted with permission from reference [92]. Copyright 2006 American Chemical Society.

Figure 4. (a) Plots of (a) magnetisation data, acquired from a SQUID magnetometer; (b) pH (red graph, left hand axis) and [OH⁻] (black line, right hand axis); and (c) T_2 relaxation time for the clock reaction between $[Co(II)EDTA]^{2-}$ and H_2O_2 (initiation at time $t = 0$). The change in magnetization observed in plot (a), after the reaction has 'clocked', is expected

to be associated with the loss of gaseous O_2, and does not have the same origin as the change in T_2 relaxation time observed before the reaction 'clocks' in plot (c). Reprinted with permission from reference [69], with permission from the Royal Society of Chemistry.

Figure 5. MRI velocity (a) and diffusion (b) maps of stationary Taylor vortices in the axial, z (i,iv), radial, r (ii,v), and azimuthal, θ (iii,vi), directions at $\omega = 1$ Hz. From reference [94], copyright 2012. Reproduced by permission of EPLA. (c) Chemical waves propagating through stationary Taylor vortices and (d) plot of effective front speed *vs.* inner cylinder rotation rate, ω. From reference [30], copyright 2010. Reproduced by permission of APS. (e) Travelling chemical waves in the BZ reaction, initiated prior to the onset of Couette flow and imaged after the formation of vortices. Adapted from reference [95].

Figure 6. MR image of a stationary chemical wave, formed by the Mn-catalyzed BZ reaction in a packed bed reactor, taken vertically in the centre of the PBR. (b) 2D velocity image, extracted from a 3D data set, of water flowing through an *xy* slice of a PBR. The interstitial velocity was 0.7 mm s^{-1}. The greyscale indicates local z velocity and the beads appear black. Reprinted with permission from reference [28] Copyright 2006 American Chemical Society.

Figure 7. Measurement of conversion within three slices, 4.5 mm apart, through a fixed-bed reactor, with slice (a) closest to the inlet. The colour scale shows the degree of conversion and it can be seen that the mean conversion increases along the direction of superficial flow, while there is significant heterogeneity in conversion within each transverse section throughout the length of the bed. Reprinted from reference [24], Copyright (2002), with permission from Elsevier.

Figure 8. Gas and liquid velocity map of SF_6 (red/yellow) and water (blue/green) during trickle flow in a packed bed reactor. The gas and liquid superficial velocities were 8.7 mm s^{-1} and 2.3 mm s^{-1}, respectively. From reference [51], copyright 2009. Reproduced by permission of Elsevier.

Figure 9. Temperature maps of the propagating chemical wave in the chlorite-thiosulfate system for the vertical (a) and the horizontal (b) cross-sections. Reprinted with permission from reference [124] Copyright 2007 American Chemical Society.

Figure 10. A time series of T_1 (left) and T_2 (right) MR images during galvanic corrosion of zinc in saturated lithium chloride solution. The distance scale is measured from the Zn wire. The time of collection is shown above each image. Reprinted from reference [139], Copyright (2010), with permission from Elsevier.

Figure 11. (a) A 2D ^{1}H MR horizontal (*xy*) image of a Zn strip in 1 M NaOH solution as a function of orientation with respect to the B_1 field. Reprinted from reference [22], Copyright (2010), with permission from Elsevier. (b) T_1 relaxation time maps from the horizontal (top) and vertical (bottom) images, during the corrosion of metallic copper in 0.5 M Na_2SO_4 solution. The corresponding total net charge passed (Q) is indicated below each image. (c) Concentration maps of Cu^{2+} from the T_1 maps shown in (b). Reprinted from reference [62], Copyright (2016), with permission from Elsevier.

Figure 12. 3D (a,c) and 2D (b,d) concentration maps of Cu^{2+} ions dissolved in 0.5 M Na_2SO_4 electrolyte following the electrodissolution of the Cu anode. The images in (a,b) were acquired after delivery of 2 mC of charge and the images in (c,d) after 16 mC of

charge. The pixel size is 500 μm (x) × 500 μm (y) × 188 μm (z), and the asterisk indicates the region on the anode that was scratched immediately prior to filling the cell with electrolyte. The 2D images in (b) and (d) are of the electrolyte layer (500 μm thick) immediately adjacent to the anode surface, and were extracted from the 3D maps shown in (a) and (c), respectively. Reprinted from reference [62], Copyright (2016), with permission from Elsevier.

Figure 13. (a) T_1 maps for a phantom sample comprising seven 5 mm NMR tubes containing NaOH solutions at a range of concentrations (0 – 10 M). (b) – (f) Horizontal ^{1}H MRI T_1 maps of a model Zn-air cell under constant load discharge at 12 kΩ. Images were acquired upon connection (b) and then at the following intervals: 11 h (c), 23 h (d), 30 h (e), until cell failure at t = 47 h (f). In images (b) to (f) the Zn strip is on the right and Ti strip is on the left. Reprinted with permission from reference [140]. Copyright 2013 American Chemical Society

Figure 14. (a) Schematic picture of the electrochemical cell. (b) 1D ^{7}Li NMR images taken over the cell, to which a constant current of 30 µA was applied. Two of the images are highlighted: one before the current was applied (t = 0; black curve) and the other after application of the current for t = 17.8 h (blue curve). (c) Concentration profile at t = 0 normalized to the RF sensitivity profile (see reference [44]) used to account for the inhomogeneity of the radiofrequency field. Reprinted with permission from reference [44]. Copyright 2012 American Chemical Society.

Figure 15. Two-dimensional [7]Li MR xy images of a Li-metal bag cell in the pristine state (a) and after passing current (b), with frequency encoding in the x direction and phase

encoding in the *y* direction. Adapted by permission from Macmillan Publishers Ltd: Nature Materials reference [43] copyright (2012)

Figure 16. ^{1}H and ^{11}B NMR spectra and CSIs of a pristine EDLC cell. (a) ^{1}H NMR spectra of the electrolyte alone (recycle delay, r.d. = 10 s) and the EDLC cell (r.d. = 4 s). (b) ^{1}H CSI of the EDLC cell with the components labelled (r.d. = 0.1 s). (c) ^{11}B NMR spectra of the electrolyte (r.d. = 10 s) and the EDLC cell (r.d. = 3 s). (d) ^{11}B CSI of the EDLC cell (r.d. = 3 s); (e) cross section through the cell design and illustration of component locations in the CSI. Reprinted by permission from Macmillan Publishers Ltd: Nature Communications reference [153] copyright (2014)

Figure 17. Velocity maps for fluid flowing in a RDE electrochemical cell, at rotation speeds of 31.4 Hz and 94.2 Hz, along the *x* (a), *y* (b) and *z* (c) directions. Reprinted from reference [166], Copyright (2015), with permission from Elsevier.

(a)   (b)   (c)   (d)

(a)　(b)

9.0
mm/s

-2.7
mm/s

(a)　(b)　(c)

10%　X　34%

gas axial velocity (mm s⁻¹)

liquid axial velocity (mm s⁻¹)

63

[Cu^{2+}] /mM

(a)

Q = 2 mC

(b)

[Cu^{2+}] /mM

(c)

Q = 16 mC

(d)

(A)

B_0

z

r

Li

LiPF$_6$ solution

Li

Cell length: 9.5 mm

⌀ : 4 mm

(C)

(B)

10 × 10^5

t = 0
t = 17.8 h

time

Intensity / a.u.

Bottom electrode, anode-side

9.5 mm

Top electrode, cathode-side

z / mm

1.5

Rel. Intensity

1

0.5

0

-5   0   5

z / mm

a

Intensity (a.u.)

2

1

0

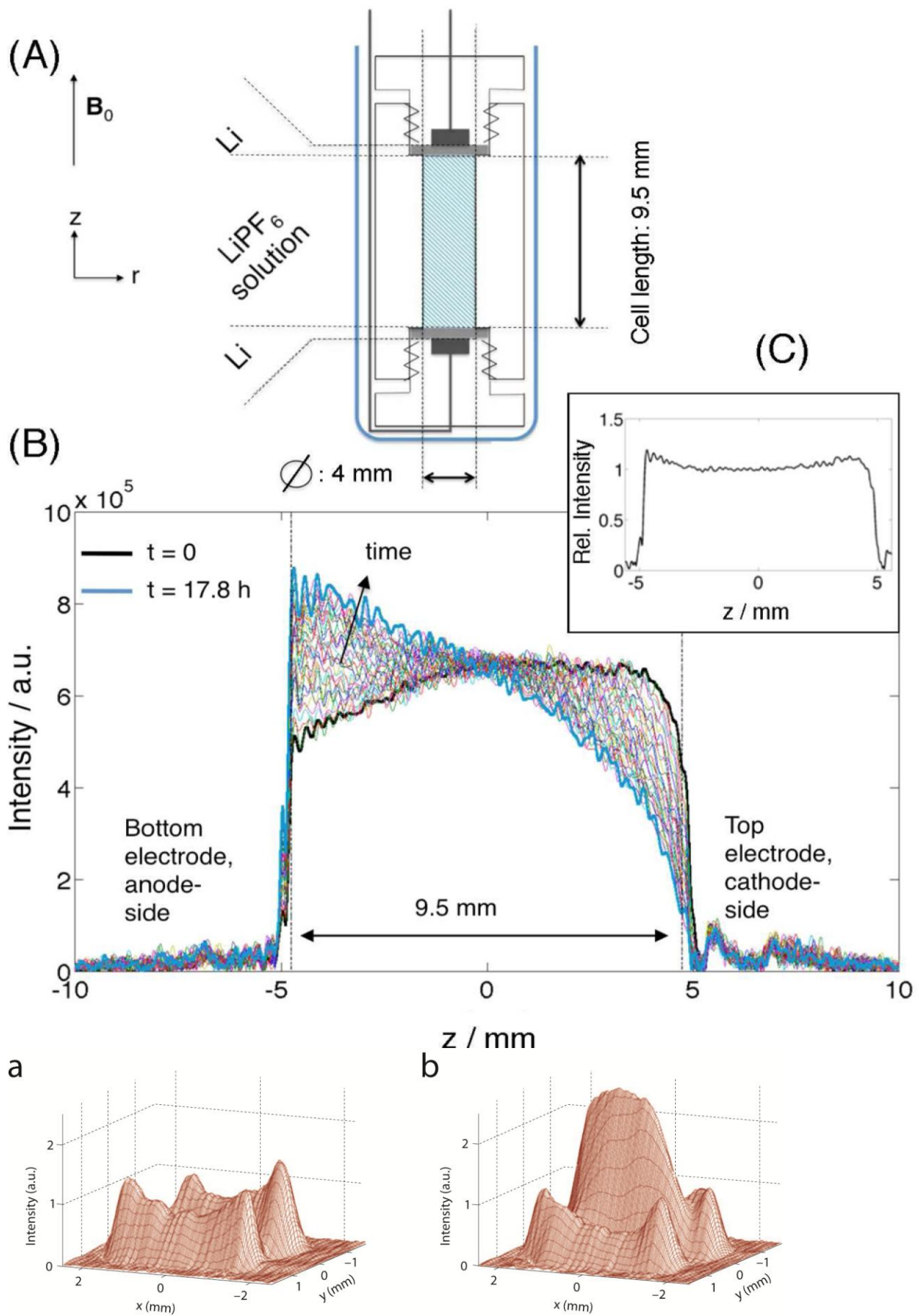x (mm)   2   0   -2
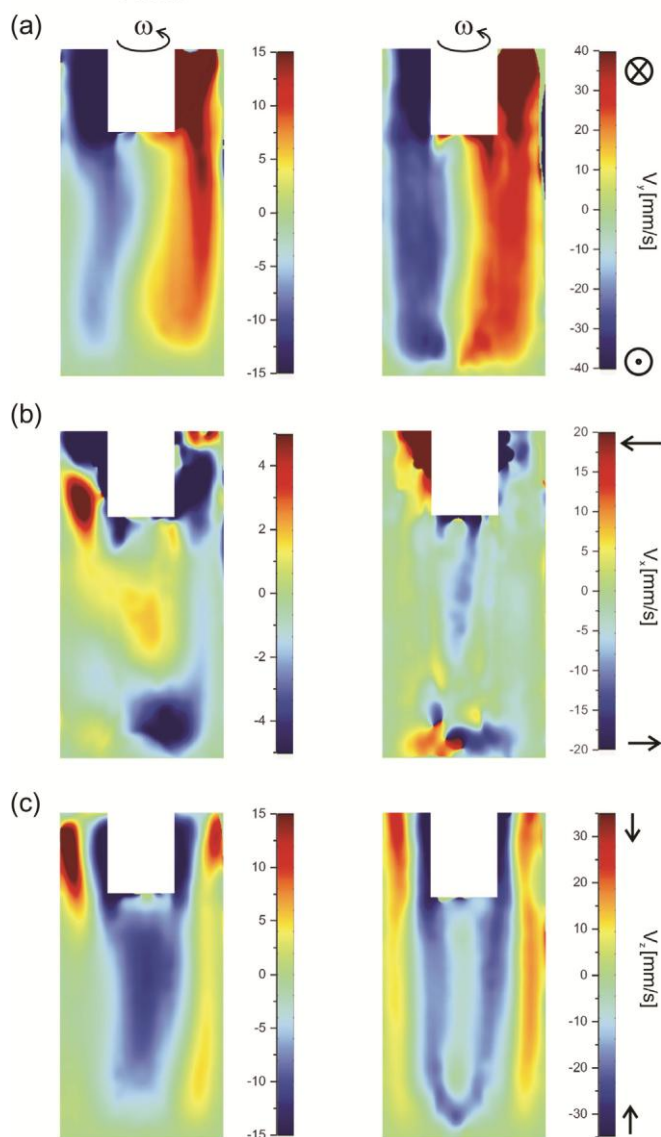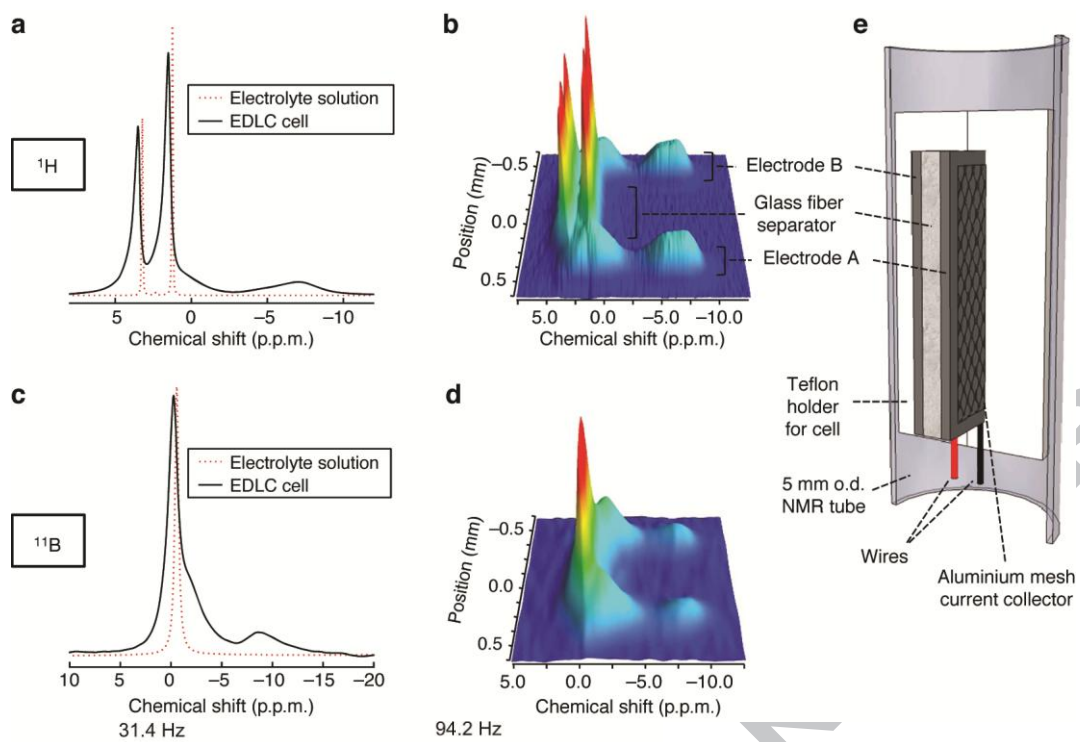
y (mm)   -1   0   1

b

Intensity (a.u.)

2

1

0

x (mm)   2   0   -2

y (mm)   -1   0   1

68

Graphical abstract

$[Cu^{2+}]$ /mM $\quad$ V_z /mm s^{-1}